

BOSTON UNIVERSITY
GRADUATE SCHOOL OF ARTS AND SCIENCES

Dissertation

**AGING EFFECTS ON THE STATISTICAL AND STRUCTURAL
PROPERTIES OF THE FORNIX OF THE BRAIN**

by

JOÃO RICARDO LEMOS RODRIGUES DOS SANTOS

B.S., Universidade do Minho, 2006

M.A., Boston University, 2010

Submitted in partial fulfillment of the
requirements for the degree of
Doctor of Philosophy

2017

© Copyright 2017, by
JOÃO RICARDO LEMOS RODRIGUES DOS SANTOS
All rights reserved

Approved by

First Reader

H. Eugene Stanley, Ph.D.
Professor of Physics

Second Reader

Douglas L. Rosene, Ph.D.
Professor of Anatomy & Neurobiology

*For all my friends, family and colleagues
who supported me through all these years.*

Acknowledgments

First, I would like to thank Ashley for all the wonderful moments we've shared and for the many more yet to come. I still can't believe how lucky I am to have met you.

I would also like to thank my family, especially my parents Ana and Avelino, for all the love and unconditional support I had throughout my life. The same applies to my brother André, despite our constant bickering while growing up. You may all be far but always close to my heart.

Finally, I would also like to thank every single person I've met throughout my journey leading here to Boston. Although you are too many to name, your presence, friendship, and valuable advice is forever treasured. I would not be who I am and where I am today without you.

AGING EFFECTS ON THE STATISTICAL AND STRUCTURAL PROPERTIES OF THE FORNIX OF THE BRAIN

JOÃO RICARDO LEMOS RODRIGUES DOS SANTOS

Boston University Graduate School of Arts and Sciences, 2017

Major Professor: H. Eugene Stanley, Professor of Physics

ABSTRACT

The brain consists of a complex network of axons, transmitting electrical impulses between interconnected neurons across distances that range from fractions of millimeters to meters. Myelinated axons, or nerve fibers, are axons that are wrapped by a myelin sheath, serving as an electrical insulation that increases the propagation speed of the signal along the nerve fiber while conserving the energy consumed and the space needed to maintain such propagation speed without myelin. Changes in the axon and surrounding myelin sheath during development and aging, or as a consequence of pathology, affect conduction and the proper functioning of the axon bundles. It is therefore important to be able to quantify the properties of these axons and their bundles and to discern which features best characterize the observed differences.

We study the effects of aging on the myelinated axons in the fornix of the brain. The fornix is the principal subcortical output tract of the hippocampal formation, which plays a central role in memory. We obtain a collection of 328 high-quality electron micrographs from the fornix of 25 different rhesus monkey brains, ranging from young adults to the elderly, with both males and females.

In this work, we develop a novel advanced recognition algorithm for automatically identifying myelinated axons and their surrounding myelin sheath. We extract multiple features of the nerve fibers and fully characterize their spatial structure. Using a feature selection algorithm, we discriminate between young and aged rhesus mon-

keys with a high level of accuracy and pinpoint the differences in the aging process at the ultrastructural level across the life span. We observe a decline in the density of myelinated axons as well as in the fraction of occupied axon area with age, while the average axon area shows no dependence on the age of the subjects. We show an increase in the myelin thickness of axons for the female subjects, while no dependence is observed for the male subjects. This sex dichotomy is also present in the g-ratio of the myelinated axons, i.e., the ratio of the axon diameter to the fiber diameter.

The method detailed here could be adapted to enable recognition in other areas as well as for changes caused by brain pathologies or by developmental disorders. Furthermore, the data collected will ultimately be useable in better modeling conduction properties in myelinated axons and better understanding how the aging process affects them.

Contents

1	Introduction	1
1.1	Background	2
1.1.1	Fornix	3
1.1.2	Myelinated Axons	4
1.2	Work Outline	4
1.2.1	Electron Microscopy	6
1.2.2	Subjects	6
1.2.3	Recognition Algorithm	6
1.2.4	Measurements	7
1.2.5	Future	7
2	Data Acquisition and Measurement Tools	8
2.1	Subjects and Image Acquisition	8
2.2	Automatic Recognition Algorithm	11
2.3	Outlier Electron Micrographs	12
2.4	Recognition Algorithm Evaluation	13
2.5	Features Measurement Tools	20
2.6	Classification and Feature Selection	24
3	Differences of Myelinated Axons with Age	27
3.1	Recognition and Characterization of Myelinated Axons	27

3.2	Single Feature Analysis	28
3.3	Feature Selection	32
3.4	Two Feature Analysis	33
3.5	Multiple Feature Analysis	34
3.6	Best Age Discriminant	35
4	Effects of Aging and Sex on the Myelinated Axons	38
4.1	Density Properties of Myelinated Axons	38
4.1.1	Dependence on age	38
4.1.2	Dependence on cognitive profile	46
4.2	Axon Areas	47
4.2.1	Distribution of axon areas	47
4.2.2	Dependence on age	49
4.2.3	Dependence on cognitive profile	53
4.3	Myelin Sheath Properties	54
4.3.1	Mean myelin thickness	55
4.3.2	Variance of myelin thickness	58
4.3.3	G-ratio	59
5	Conclusions	66
A	Calculation of the Orientation Angle and Flattening of each Contour	71
A.1	Image Moments	71
A.2	Calculate Image Moments	73
B	Circular Statistics	75
B.1	Angular Average	75
B.2	Circular Distributions	76
B.3	Orientation Angles	78
B.4	Orientalional Order Parameter	79

C	Outliers	82
C.1	Probability Plot	82
C.2	Box Plot	82
C.3	Permutation Test	85
C.4	Summary	85
D	Nearest Neighbor Mean Distance for a Poisson Point Process	88
	Bibliography	92
	Curriculum Vitae	103

List of Tables

2.1 List of the rhesus monkeys 10

List of Figures

1.1	Illustration of the fornix of the brain	3
1.2	Myelinated axon illustration	5
2.1	F_1 scores in function of age	16
2.2	Recognition rates in function of age	17
2.3	F_1 scores separated by sex and age group	17
2.4	Recognition rates separated by sex and age group	18
2.5	Overlap ratio in function of age	19
2.6	Effective local density calculation	22
3.1	Processing steps for characterizing myelinated axons	29
3.2	Single feature analysis	30
3.3	Locations of the fornix samples in a two features space	36
4.1	Axon density in function of age	39
4.2	Axon density in function of age, separated by sex	39
4.3	Axon density separated by sex and age group	40
4.4	Number of axons in function of age	41
4.5	Number of axons in function of age, separated by sex	42
4.6	Number of axons separated by sex and age group	42
4.7	Fraction of occupied axon area in function of age, separated by sex	43
4.8	Fraction of occupied axon area separated by sex and age group	44
4.9	Fraction of occupied fiber area in function of age, separated by sex	45

4.10	Fraction of occupied fiber area separated by sex and age group	45
4.11	Axon density in function of CII	46
4.12	Distribution of axon areas	48
4.13	Axon areas in function of age, separated by sex	51
4.14	Axon areas separated by sex and age group	51
4.15	Axon areas dispersion in function of age, separated by sex	52
4.16	Axon areas dispersion separated by sex and age group	53
4.17	Axon areas in function of CII, separated by sex	54
4.18	Myelin thickness in function of age	55
4.19	Myelin thickness in function of age, separated by sex	56
4.20	Myelin thickness separated by sex and age group	57
4.21	Myelin thickness in function of CII	58
4.22	Variation of myelin thickness in function of age, separated by sex	59
4.23	Variation of myelin thickness in function of CII, separated by sex	60
4.24	Illustration of g-ratio	61
4.25	G-ratio in function of age	62
4.26	G-ratio in function of age, separated by sex	63
4.27	G-ratio separated by sex and age group	64
4.28	G-ratio variation in function of age, separated by sex	64
4.29	G-ratio variation in function of age, separated by sex	65
B.1	Example of a wrapped normal distribution	77
B.2	Orientalional order parameter vs. orientational standard deviation	80
C.1	Probability plot of the images mean orientational order parameter	83
C.2	Probability plot of the subjects mean orientational order parameter	83
C.3	Box plot of the subjects mean orientational order parameter	84
C.4	Permutation test of orientational order parameter vs. mean flattening	86
C.5	Permutation test of orientational order parameter	87

List of Abbreviations

CII	Cognitive Impairment Index
CNS	Central Nervous System
EM	Electron Microscopy
EMs	Electron Micrographs
FN	False Negatives
FP	False Positives
HI	Hexagonality Index
IQR	Interquartile Range
MRI	Magnetic Resonance Imaging
PCA	Principal Component Analysis
PDF	Probability Density Function
PI	Poligonality Index
PNS	Peripheral Nervous System
PPV	Positive Predictive Value
ROI	Region of Interest
TP	True Positives
TPR	True Positive Rate
UC	Circular Uniform Distribution
WN	Wrapped Normal Distribution

Chapter 1

Introduction

In this chapter we explain the topic being studied in detail and supply a biological review of nerve fibers and the fornix, explaining its importance in predicting impairments in memory function that occur with age.

The nervous system is a complex network allowing the transmission of signals between interconnected neurons across distances which vary from fractions of millimeters to meters. Axons following similar paths are often bundled together, forming nerves in the peripheral nervous system and tracts in the central nervous system such as the corpus callosum which interconnects the two brain hemispheres. The proper functioning of such tracts depends on axon characteristics such as size, density and spatial organization. The axons populating different tracts or bundles change during development [1, 42–48] and aging [2, 49–53], as well as a consequence of pathology [54–65] and environmental influences [66–68]. Alterations in specific genes might also influence the organization of bundles of axons [43, 69, 70]. It is therefore important to have a means for quantifying, in an objective manner, the characteristics of these axons and their bundles and to discern which features best characterize the observed differences. Understanding the ultrastructure of axons, i.e. the structure at scales of the nanometers, is a critical issue for understanding the nervous system and the human connectome.

Typically, studies of differences observed in nerve fibers are limited to one or just a few geometrical properties, chosen to measure an evident and already observed difference. They then statistically evaluate that difference between groups, in an individual fashion. This methodology presents several problems, as some of the differences may be subtle and not easily identified by visual inspection and hence not chosen for quantification, restricting the identification of potential differences. As a result, there have been few systematic attempts to analyze and explore a wide range of possible features as a means to identify the main effects [71–74].

We present here a new method to uncover which features of axons are most affected by an underlying biological process. In this systematic investigation, we consider *a priori* a large set of candidate features representative of diverse types of possible differences in axons (e.g., density, shape of axons, spatial order, etc.) and then use the feature selection technique [3,4,75] to identify which combinations of such features yield the best discrimination between axons of two distinct groups. This approach enables the identification from the list of candidate features, of the *set* of features that, when taken *together*, best discriminates between groups in a general dataset.

As a case study, we apply this methodology to characterize changes observed with normal aging in the myelinated nerve fibers of the fornix of young and old rhesus monkeys. The fornix is a bundle of nerve fibers carrying signals from the hippocampus to other structures in the limbic system, such as the hypothalamus, and it is crucial in normal cognitive functions, especially memory formation [76]. Previous studies have shown that the axon density declines with age [5].

1.1 Background

In this chapter we summarize the current understanding of the research topic.

1.1.1 Fornix

The fornix of the brain is the principal subcortical output tract of the hippocampal formation, which plays a central role in memory functions. Being true to its name, originated from the Latin word *arch*, it is C-shaped, as shown in Fig. 1.1. This axon tract is the largest pathway interconnecting the hypothalamus and the hippocampus [6,7], best seen from the medial surface of the divided brain. Fornix damage has been shown to permanently impair new learning and memory [6]. Hence, this bundle of nerve fibers is a potential contributor to the changes that are predictive of the impairments in memory function that occur with age.

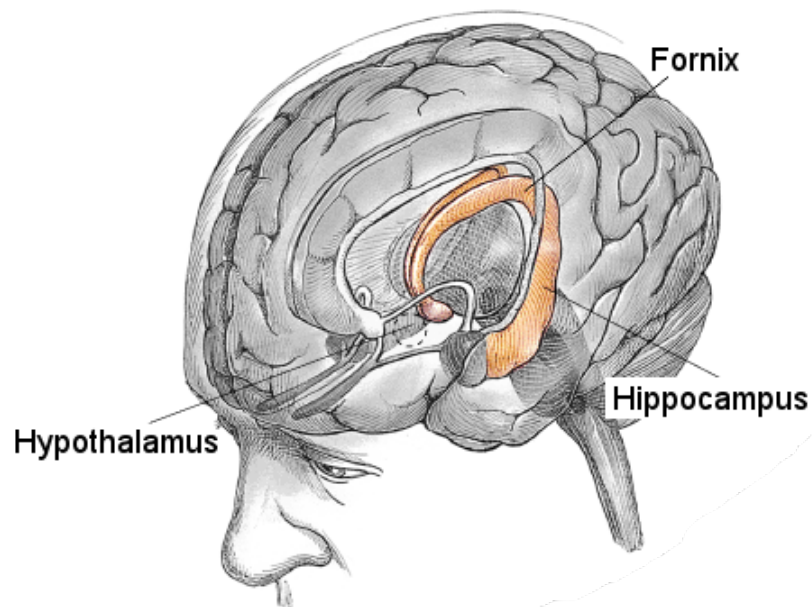


Figure 1.1: Illustration of the fornix in a human brain. The fornix of brain is highlighted in orange in this illustration of the human brain. It is a bundle of nerve fibers forming an arch, carrying signals from the hippocampus to distal brain sites of the limbic system.

1.1.2 Myelinated Axons

Axons are projections of neurons, with the purpose to conduct electrical impulses between different neurons. Myelinated axons, in particular, are axons that are wrapped by a myelin sheath, originating from oligodendroglial cells in the central nervous system (CNS), as illustrated in Fig. 1.2, or Schwann cells in the peripheral nervous system (PNS). This myelin sheath serves as an electrical insulation that increases the propagation speed of the signal along the nerve fiber while conserving the energy consumed and the space needed to maintain such propagation speed without myelin. If axons in the human spinal cord were unmyelinated, the spinal cord would need to be as large as a tree trunk to maintain similar conduction speeds. Because changes in the myelin sheath affect conduction, communication among neurons depends upon both axon integrity and the integrity of the myelin sheath enclosing it. When the axons and surrounding myelin change during development and aging, or change as a consequence of pathology, the functioning of the axon bundles also changes. Changes in the myelin sheath alone alter action potential conduction during development across the adult life span and into old age as well as in a variety of neurological conditions such as multiple sclerosis.

During the normal aging process, myelinated axons (or nerve fibers) in the fornix area of the rhesus monkey brain decrease in number [5,8]. It has also been observed that the myelin degeneration increases with age [5,8].

1.2 Work Outline

We study the ultrastructure of myelinated axons in electron micrographs (EMs) at a level of resolution not possible with optical microscopy. To accomplish this objective, we analyzed electron microscopy images using new approaches from statistical physics to identify age-related changes in the axon and in its myelin sheath.

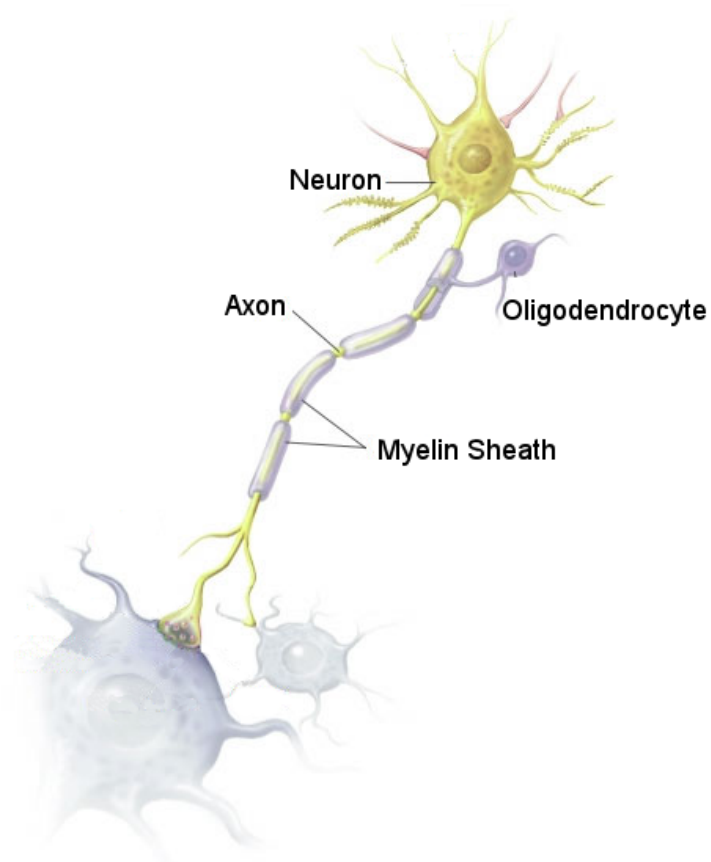


Figure 1.2: Illustration of a myelinated axon in the central nervous system. The myelinated axon is a projection of the neuron that is wrapped by an insulating layer called the myelin sheath. In the case of the central nervous system, the myelin sheath originates from a glial cell called oligodendrocyte.

1.2.1 Electron Microscopy

While there are a variety of light microscopic approaches that visualize axons and/or myelin, none of these allow careful study of the axon and myelin sheath in detail and in relationship to each other. In fact, the level of resolution achieved with optical microscopy is not sufficient for a detailed study of the axons and myelin sheath. This detailed study can only be accomplished with ultrastructural analysis using electron microscopy (EM). However, this poses challenges as superb optimal fixation and processing are required. Samples are also restricted in spatial location and limited in number.

1.2.2 Subjects

An archive of available electron micrographs were prepared from optimally fixed rhesus monkey brains. These EMs were prepared in the laboratory of Dr. Alan Peters and were taken from the fornix of the brain of superbly fixed and prepared rhesus monkey brains, both males and females and ranging from young adults to the elderly [5, 8]. These monkeys had also been behaviorally evaluated for cognitive aging [9]. A total of 328 electron micrographs from the fornix of 25 different rhesus monkey brains were digitized.

1.2.3 Recognition Algorithm

It is extremely slow to quantify features from these samples in sufficient numbers to make solid inferences. Therefore, we developed an advanced feature recognition algorithm that can be successfully applied to automatically identify axons and extract multiple different features that accurately discriminate between young and aged rhesus monkeys [10]. We expanded upon this model by developing novel recognition algorithms to identify the myelin sheath surrounding the myelinated axons, as well as to quantify the myelin sheath properties of myelinated axons in the fornix.

1.2.4 Measurements

These algorithms produce quantitative measurements of individual axon properties such as the cross-sectional area as well as the shape in relationship to the thickness and the shape of their myelin sheaths. Structural properties between myelinated axons are also measured in order to uncover possible relationships between neighboring axons. We measure quantities such as the average thickness of the myelin sheath, the distribution of these thicknesses, and the relationship to the axon diameter (i.e., g-ratio). We determine how the ratio of axon diameter to myelin sheath thickness differs across adult development.

Furthermore, we apply a feature selection approach to identify the most pertinent features in distinguishing axons from subjects of different ages. With these measurements from subjects of different ages and sexes, we determine if there are differences in the aging process at the ultrastructural level across the life span, as well as in different cognitive profiles.

1.2.5 Future

The data regarding the ratio of axon diameter to myelin sheath thickness gathered from the developed recognition algorithms could be used to model conduction properties in these myelinated axons.

It could also be valuable for modeling different properties of diffusion magnetic resonance imaging (MRI) of white matter and axons.

This method could also be adapted to enable the recognition in other imaging modalities of changes caused by brain pathologies in neurodegenerative diseases, such as Alzheimer's Disease, or by developmental disorders.

Chapter 2

Data Acquisition and Measurement Tools

2.1 Subjects and Image Acquisition

For this study we used an archive of available electron micrographs (EMs) of optimally fixed rhesus monkey (*Macaca mulatta*) brains from the collection of Dr. Alan Peters [5, 11]. The EMs used in this study were prepared in the laboratory of Dr. Alan Peters and were taken from the fornix of the brain of superbly fixed and prepared rhesus monkey brains, both male and female, ranging from young adults to the elderly [5, 8, 11]. These same subjects had previously been behaviorally evaluated for cognitive aging [9], and a measure of cognitive impairment was obtained.

The experimental setup for fixing the brains of the monkeys, including the tissue preparation and microscopy setup, is described in detail in Ref. [11]. All procedures regarding the care and death of these monkeys followed the standards set by the National Institutes of Health *Guide for the care and use of laboratory animals*. For this procedure, the monkeys were anesthetized until reaching a state of areflexia, intubated and respirated with a mixture of CO₂ and O₂, and finally perfused intraaortically with a warm solution of 1.25% glutaraldehyde and 1.0% paraformaldehyde in

0.1 M cacodylate or phosphate buffer at a pH value of 7.4. After their death, the brain was removed and separated by the mid sagittal plane, splitting the two brain hemispheres. The brain hemispheres were fixed by immersing them in a cold solution of 2% paraformaldehyde and 2.5% glutaraldehyde in the same buffer used for the perfusion and stored.

In order to obtain samples of the fornix for analysis in electron microscopy, one of the hemispheres of each monkey was selected and a section of approximately 3 mm was cut along the coronal plane (also called frontal plane) passing through the thalamus, the bisected corpus callosum and the body of the fornix. A block containing the fornix was removed from this section and posteriorly postfixed in 1% osmium tetroxide, dehydrated, and embedded in Araldite resin.

For the electron microscopy, thin sections containing the lateral portion of the fornix were trimmed from this block, as the entire cross-section of the fornix is too large to fit onto an EM grid. These sections were cut using an ultramicrotome taking care that the nerve fibers of the fornix were cross-sectioned perpendicularly to their length. Afterwards, these thin sections were stained with uranyl acetate and lead citrate.

The thin cross-sections of the lateral portion of the fornix were mounted on 200 mesh grids (with holes of approximately $100\ \mu\text{m}$ in length) and electron micrographs were taken at a magnification of $5000\times$. The electron micrographs were taken systematically every third opening of every third row of the mesh grid, effectively every ninth hole of the mesh grid.

A total of 328 high-quality EMs were taken from the fornix of 25 different rhesus monkey brains, 14 of them males and the remainder 11 females. Our cohort is divided into two groups: a young adult group, for subjects with ages ≤ 15 years; and an old adult group for subjects of > 15 years of age. We chose the age of 15 years as the separation between the two age groups, since most biological development in the rhesus monkeys is over as they turn 15 years of age. Any effects of aging would

start showing from this age. Similar age classification procedures have been used in other works [5, 12, 13]. Our cohort is thus divided into two age groups: a young adult group, consisting of 12 subjects (7 males and 5 females) with ages ranging from 3.8 to 14.9 years, and an old adult group composed of 13 monkeys (7 males and 6 females) aged between 18.4 and 33.1 years old. Table 2.1 lists the animals used in this study, together with their age and sex.

Animal number	Sex	Age (years)	Age group	CII
AM058	M	3.8	young	no data
AM007	M	5.1	young	no data
AM076	F	6.4	young	0.08
AM077	F	6.4	young	2.269
AM129	F	6.7	young	1.865
AM130	F	7.7	young	1.282
AM047	M	9	young	-0.51
AM096	F	9	young	2.123
AM053	M	9.6	young	0.319
AM042	M	12.2	young	0.95
AM140	M	12.4	young	no data
AM144	M	14.9	young	0.417
AM221	F	18.4	old	1.799
AM101	M	18.9	old	4.21
AM209	M	19.2	old	0.753
AM133	M	19.5	old	2.463
AM178	F	22	old	6.2
AM019	F	24.7	old	1.977
AM100	F	24.7	old	3.588
AM062	M	27.5	old	3.806
AM027	M	27.9	old	1.242
AM023	F	30.8	old	6.748
AM091	M	31.5	old	0.25
AM041	F	31.9	old	4.512
AM018	M	33.1	old	no data

Table 2.1: List of the different rhesus monkeys used in this study with their corresponding animal number, sex, age, age group, and cognitive impairment index (CII) [5, 9].

These EM images were digitized with a resolution of 237 pixels per micron.

2.2 Automatic Recognition Algorithm

A reliable statistical analysis of the myelinated axons present in the fornix depends on the recognition of a sufficiently large number of axons, from a large set of electron micrographs. Considering the large number of myelinated axons (approximately 150 for each electron micrograph), we developed an automated image recognition algorithm to extract the coordinates and boundaries of the myelinated axons as well as their surrounding myelin sheath, with the highest accuracy possible.

In the EM images, the axon is very lightly stained, while the myelin sheath surrounding it is the darkest feature in the image. Our algorithm takes advantage of this contrast and searches for continuous boundaries between a convex bright region and dark region. Note that the recognition procedure used here is original, and it is based on well-founded assumptions based on morphologic facts [14].

The steps involved in the recognition algorithm are:

1. We smooth the image using a Gaussian filter with a standard deviation of 6 pixels ($\sim 0.025 \mu m$);
2. binarize the image using a threshold that varies for different samples, leaving only myelin/non-myelin objects;
3. find the edges using a Canny edge detector [86];
4. extract contiguous regions with area larger than 5000 pixels ($\sim 0.089 \mu m^2$) – this is a cut-off on the object's area implemented in order to eliminate false positives due to speckles;
5. discard regions that have the ratio of perimeter to square root of area larger than 6.2 – this is a cut-off on circularity;
6. discard regions where the ratio between the standard deviation and the mean intensity of the pixels is larger than 0.5 – this is a cut-off on uniformity;

7. given the typical morphologic features of myelinated axons, discard regions with contours having three or more large values of convex curvature. We consider $0.03 \text{ pix}^{-1} (\sim 7.11 \mu\text{m}^{-1})$ as a large value of convex curvature. This eliminates false positives recognized in areas surrounded by the myelin sheaths of other axons.

Finally, in order to have the highest possible accuracy, a manual check is performed to eliminate remaining false positives and to mark possibly missed myelinated axons.

2.3 Outlier Electron Micrographs

In the EM images, the cross-section of a myelinated axon typically has an elliptical shape with some degree of elongation. These different elliptical shapes could be the result of a small variation of the longitudinal axis of the individual myelinated axons in the fornix in a way that the cross-sectional cut is not perfectly perpendicular to this axis. This variation is typically small and, taking all the axons of the fornix into consideration, the cross-sectional cut is perpendicular to the average longitudinal axis of the fornix. However, in certain EM images all myelinated axons display the same axes of elongation in its cross-section, i.e., the orientation angles of the axes of elongation for each cross-section of a myelinated axon have very little dispersion around a central value orientation value. This lack in dispersion could be the result of a possible bias in the angle of the cut of the myelinated axons, wherein the cut was done at an angle to the average longitudinal axis of the fornix. The method of calculation of the orientation angle of the cross-sectional area of the myelinated axon is shown in more detail in Appendix A.

Considering this could introduce a bias in our measurements, we developed a method to identify possible subjects with cross-section shapes with a high degree of elongation (measured via its flattening) and with low variation in the orientation angle of the cross-section shapes [15, 16] around its central angle (measured via its

orientational order parameter). We explain in detail the meaning of the orientational order parameter and how it is calculated in Appendix B.

We determined that the myelinated axons in subjects AM019 and AM144 have large flattening values (a measure of elongation of an elliptical shape), showing a higher probability of these axons having been cut at an angle, instead of perpendicularly. These 2 subjects also have the highest values for the average orientational order parameter (measuring the dispersion of these orientation angles around a central value).

Using a permutation test, wherein we randomly shuffle the labels for each EM image and recalculate the orientational order parameter, we conclude that these 2 subjects, AM019 and AM144, are significantly distinct from the rest of the subjects with $p < 10^{-4}$ and should be ignored from our analysis. This analysis was confirmed by plotting the orientational order parameters in a Tukey box plot and classifying any data point outside the region $[Q_1 - 1.5 \times IQR, Q_3 + 1.5 \times IQR]$ as an outlier. In this case, Q_1 and Q_3 are the 1st and 3th quartile respectively, while IQR is the interquartile range, defined as $IQR = Q_3 - Q_1$. In a normal distribution, this criterion would classify 0.70% of all data points as outliers. According to this method, the data points from the subjects AM019 and AM144 are outside the region and classified as outliers. A more detailed explanation of these calculations is present in Appendix C.

2.4 Recognition Algorithm Evaluation

In order to evaluate the recognition algorithm for myelinated axons, we manually corrected all the algorithm contours, adding axons it had missed (false negatives), eliminating non-axons the algorithm had recognized (false positives), and correcting the contours to match the axolemma, i.e., the membrane limiting the axon. These manually corrected axon contours were done for 4 EM images per subject, and used to quantify the performance of the recognition algorithm.

Region of Interest

The EM images were digitized from the electron micrographs into images of 3240×4800 pixels, with a resolution of 237 pixels per micron. Considering the axons present in the border of the EM image are not fully represented, we select a Region of Interest (ROI), defined as the region with uniform density of axons centroids, i.e., their center of mass. This way, we avoid including recognized axons that are not fully drawn in the EM image, due to size limitations of the electron micrographs. In our case, we select the ROI as the center region with dimensions 2800×4100 pixels, which corresponds to an area of $205 \mu m^2$. All calculations involve only myelinated axons with centroids inside the ROI.

Sensitivity, Precision and F1 score

In a good recognition algorithm, one wants to minimize the number of false positives (FP), i.e., the number of recognized elements that are not axons, while also minimizing the number of false negatives (FN), i.e., the number of actual axons that the recognition algorithm failed to recognize. The performance of the recognition algorithm can be evaluated by calculating the True Positive Rate and Positive Predictive Value.

The True Positive Rate (TPR), also called sensitivity or recall, is defined as the fraction of all actual axons that are recognized. In mathematical terms, it is defined by the equation

$$\text{TPR} = \frac{\text{TP}}{\text{TP} + \text{FN}}, \quad (2.1)$$

where FN is the number of false negatives missed by the recognition algorithm, and TP is the number of true positives, i.e., the number of recognized axons that match the actual axons. In our calculations, we defined an algorithm contour to be a true positive if it overlapped with an actual axon.

The Positive Predictive Value (PPV), also called precision, is defined as the frac-

tion of all recognized elements that are actual axons, defined by

$$\text{PPV} = \frac{\text{TP}}{\text{TP} + \text{FP}}, \quad (2.2)$$

where FP is the number of false positives given by the recognition algorithm.

A good recognition algorithm balances these 2 quantities so as to recognize the maximum number of axons, without sacrificing its precision by recognizing false instances as axons. This balance is measured by calculating the F_1 score, the harmonic mean of the precision and the sensitivity, defined as

$$F_1 = \frac{2}{\frac{1}{\text{TPR}} + \frac{1}{\text{PPV}}}. \quad (2.3)$$

For the 23 subjects analyzed, we compared the manually corrected contours with the algorithm contours of the myelinated axons. Accordingly, our recognition algorithm of myelinated axons has an average positive predictive value of 95%, i.e., 95% of the recognized axons are actual axons. This translates into a false discovery rate ($\text{FDR} = 1 - \text{PPV}$) of 5%. Additionally, the recognition algorithm has an average value of 90% for true positive rate, i.e., it recognizes 90% of the actual axons.

Taking these 2 quantities into account, we calculate that our recognition algorithm has an average F_1 score of 0.922. These recognition rates are limited by the overlap in the pixel values between the myelin sheath pixels and the axon pixels. The greater the overlap, the worse the recognition rate typically is.

An advantage of our myelinated axon recognition algorithm is that the recognition rates show no significant correlation with the age of the subjects, having similar rates for both age groups (young and old), as shown in Fig. 2.1. Therefore, the algorithm performance is not dependent on the age of the subjects analyzed.

This age-independent performance of the recognition algorithm is also confirmed by the fact that both TPR and PPV rates are also not dependent of the age the

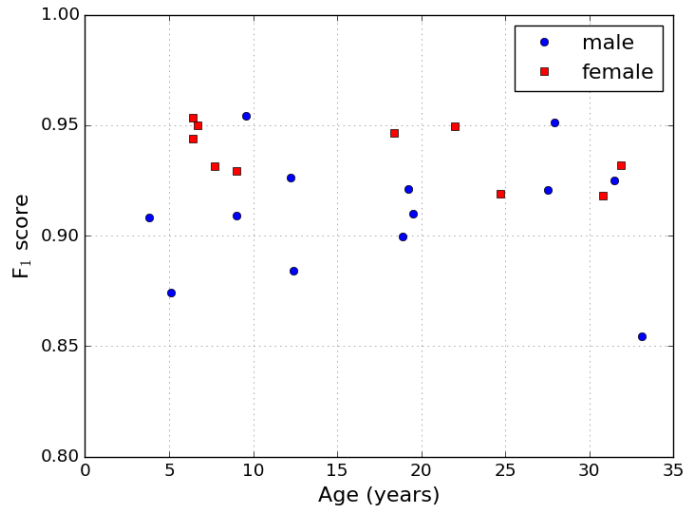


Figure 2.1: F_1 scores of the myelinated axon recognition algorithm in function of age, stratified by sex. The Pearson correlation coefficient for all subjects is $R = -0.14$ with $p = 0.52$ ($N = 23$). The Pearson correlation coefficient for the male subjects is $R = 0.016$ with $p = 0.96$ ($N = 13$), while for the female group we get $R = -0.55$ with $p = 0.10$ ($N = 10$).

subjects, as illustrated in Fig. 2.2.

When separating by age group, we also do not detect a significant difference between young male and young female subjects, or between old male and old female subjects.

However, we do observe that female subjects have consistent higher TPR values than the male subjects ($p = 9.1 \times 10^{-4}$ for a two-sided Mann–Whitney U test), i.e., the algorithm recognizes a higher percentage of the myelinated axons for the female subjects. On average, the female subjects have a TPR of 92.8%, while male subjects have an average TPR of 87.5%.

A closer look into the EM images of this age group reveals that there is an increased overlap in the pixel values between the myelin pixels and the axon pixels for the male subjects, resulting in a lower contrast and, therefore, a lower TPR, compared to the female subjects. This difference is not dependent with how long ago the subjects were perfused, since the TPR values are not correlated with the date of perfusion.

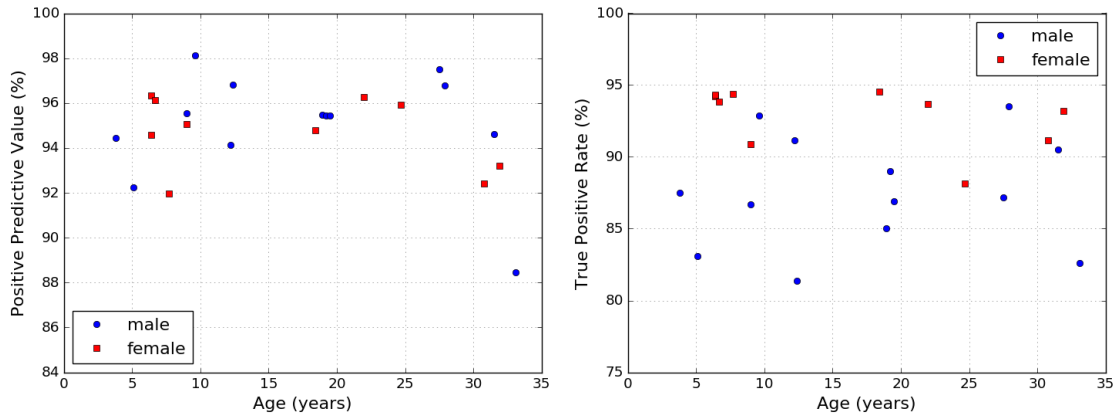


Figure 2.2: Positive Predictive Values (left) and True Positive Rates (right) of the myelinated axon recognition algorithm in function of age, stratified by sex. Both quantities show no correlation with age when considering all the subjects. When separating by sex, both PPV and TPR have no significant correlation with age.

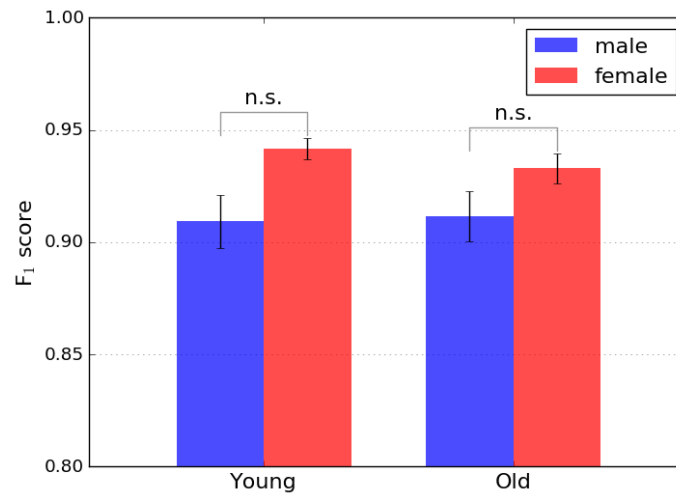


Figure 2.3: F_1 scores of the myelinated axon recognition algorithm for the 2 age groups, stratified by sex. For each age group, a two-sided Mann–Whitney U test was performed on the F_1 score values of all male and female subjects in that age group. In this figure, n.s. stands for not significant.

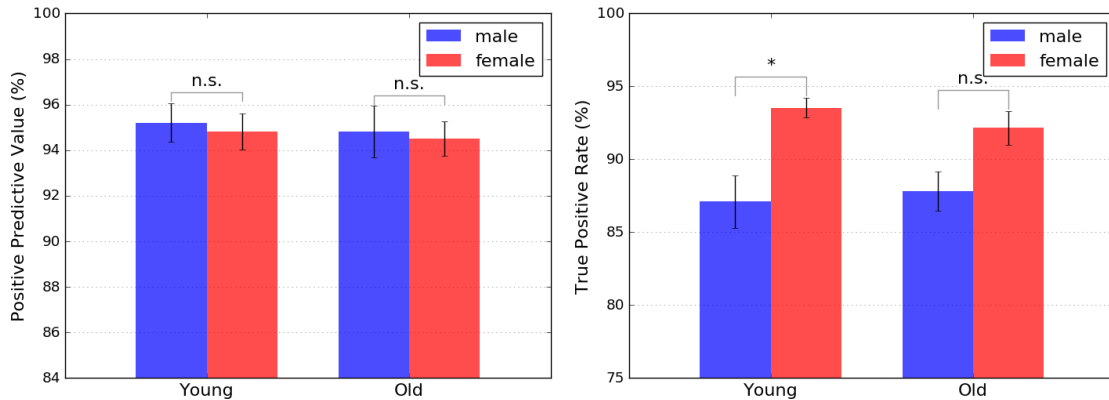


Figure 2.4: Positive Predictive Values (left) and True Positive Rates (right) of the myelinated axon recognition algorithm for the 2 age groups, stratified by sex. For each age group, a two-sided Mann–Whitney U test was performed on the recognition rates of all male and female subjects in that age group. There is a statistical significant difference in the TPR values between the young males and young females ($p = 0.023$).

Note that this difference is only observed on the TPR values, and not the PPV values. Therefore, we have similar rates of false positives for all subjects, independently of their age or sex. As such, any measurement of the individual axon properties would not suffer from a bias, since it would be affected by the same small false discovery rate of 5%, i.e., the number of falsely classified axons by the recognition algorithm. Nevertheless, we manually eliminated the few remaining false positives and marked any missing myelinated axons, so any sex difference in the TPR values would not affect the final results observed.

Overlap Ratio

We also evaluate the recognition algorithm by how well it captures the shape of the axon. A good recognition algorithm has the algorithm contours as close to the actual borders of the axons, i.e., the axolemma. In this case, the areas of the recognized axon and the actual axon should be as close as possible.

We measure how close these contours are by calculating the overlap ratio. The overlap ratio is defined by the ratio of the overlapped area between 2 contours (i.e.,

their intersection) to the total area occupied by at least one of the contours (i.e., their union). The overlap ratio values range between 0 and 1, where a ratio of 0 means no overlap while a ratio equal to 1 means a perfect match. For each recognized axon that matches an actual axon, i.e., a true positive, we calculate this overlap ratio.

Comparing the manually corrected axon contours with the algorithm axon contours, we calculated that the recognition algorithm axon contours have, on average, an overlap ratio of 0.918. As a comparison, when we match the contours manually drawn by 2 different persons, they have an average overlap ratio in the range of 0.93–0.94. Thus, the algorithm contours of the recognized myelinated axons match well to the contours of the actual axon.

Similarly to the recognition rates, the overlap ratio values have no correlation with the age of the subjects, as illustrated in Fig. 2.5. Therefore, our recognition algorithm is independent of age, since not only its recognition rates but also their contours do not depend on the age of the subjects analyzed.

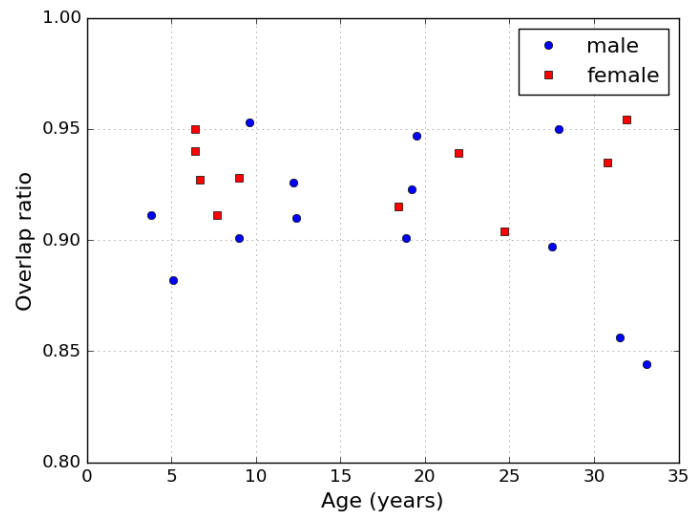


Figure 2.5: Overlap ratio values of the myelinated axon recognition algorithm in function of age, stratified by sex. The Pearson correlation coefficient for all subjects is $R = -0.22$ with $p = 0.31$ ($N = 23$). The Pearson correlation coefficient for the male subjects is $R = -0.36$ with $p = 0.23$ ($N = 13$), while for the female group we get $R = 0.10$ with $p = 0.78$ ($N = 10$).

2.5 Features Measurement Tools

In the following we describe the quantities that we consider for our analyses. We determine the density and other quantities related to density (e.g., fraction of occupied area). This allows us to test our axon recognition procedure against the manual procedure used in Ref. [5] in which the density of myelinated axons was previously determined. We note that a reduction in the number of myelinated axons upon aging was previously observed [5, 87–89].

Starting from the positions of the centroids \mathbf{R}_i of the myelinated axons in our samples, we can also calculate different quantities related to their structure. The first one is the distribution of nearest-neighbor distances, which can be plotted by building the histogram of the distances of the closest axon to every axon in the sample. Similarly, the n -th nearest neighbor distance distributions can be obtained from the histogram of the distances to the n -th neighbor.

The n -th nearest distribution is also used to calculate the effective local density of the sample. For a random set of points in an area (i.e., a random particle distribution described by a homogeneous Poisson point process) with an uniform mean density $\rho > 0$, the mean distance of the n -th nearest neighbor $\langle r_n \rangle$ is given by [90–92]

$$\langle r_n \rangle = \frac{1}{\sqrt{\pi\rho}} \frac{\Gamma(n + 1/2)}{\Gamma(n)}, \quad (2.4)$$

where $\Gamma(n)$ is the Gamma function (see Appendix D for details). For large n , this exact formula can be approximated by

$$\langle r_n \rangle \approx \sqrt{\frac{n}{\pi\rho}}, \quad (2.5)$$

with a relative error smaller than 1.6% for $n \geq 8$. Although Eq. (2.5) was derived for a random set of points, this power law behavior for sufficiently large n is also observed in our samples.

Considering Eq. (2.5), we expect the n -th nearest neighbor distance to increase with rank n according to a power law. Therefore we can estimate the density of the system by fitting a line for large n on the log-log plot of the n -th nearest neighbor distance versus the rank n . We fit a line for the points $n = 8, 9, \dots, 15$ and calculate this “regression” density (called the effective local density) from the intercept of the linear regression. Figures 2.6(a) and 2.6(b) show two samples with equal densities but different effective local densities due to the presence of a large axon-free region. The calculation of the effective local density is illustrated in Fig. 2.6(c) for the two particular samples shown in Figs. 2.6(a) and 2.6(b). Note that the effective local density is calculated from the nearest neighbor distance behavior and, as such, it provides a measure of the local density around axons.

We also construct the Voronoi tessellation of the embedding space as determined by the spatial distribution of the centroids of the myelinated axons and study the statistical and morphologic properties of the Voronoi cells of area \mathcal{A}_i , see Fig. 3.1. In the Voronoi tessellation, given a discrete spatial distribution of points \mathbf{R}_i , here identified with the centroids of the axons, the Voronoi cell associated to the point \mathbf{R}_i is defined as the set of points closer to the point \mathbf{R}_i than to any other point of the distribution. In practice, all the space is divided into convex non-overlapping polygons built around each centroid where each polygon edge bisects the line segments joining the respective centroid to its neighbors (i.e., a Delaunay triangulation). An interesting concept that can be investigated starting from the position of the axon \mathbf{R}_i and the Voronoi tessellation of the embedding space is the polygonality index (PI), first defined in Ref. [80]. The PI measures how close the symmetry of the sample is to a well-known ordered structure. In this case we compare our samples to a regular triangular lattice, which corresponds to the 2D lattice of equal disks with the highest density. Its Voronoi tessellation is a hexagonal tiling. Following Ref. [80], for each point \mathbf{R}_i (centroid of the axon) in the tessellation we measure the adjacent angles between line segments joining \mathbf{R}_i with the centers of neighboring Voronoi cells, i.e.,

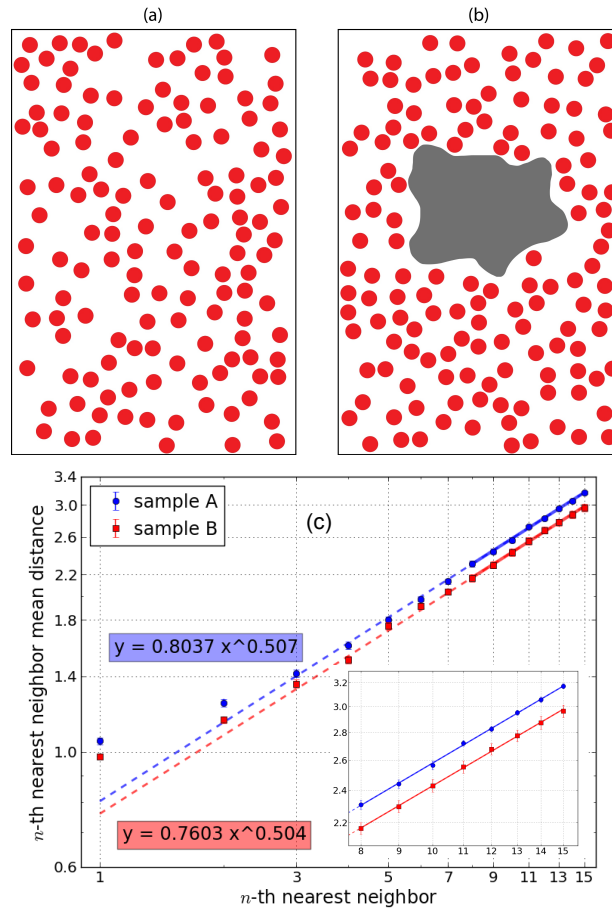


Figure 2.6: Effective local density calculation. (a) and (b) Illustrations of samples with equal densities ($\rho = 0.50$) but different effective local densities. The sample in figure (a) has an effective local density value of 0.49, similar to its density value, while the sample in figure (b) has a higher effective local density value of 0.55, resulting from the axons (in red) being closer together due to the presence of a large axon-free region (in gray). (c) Plot of the average n -th nearest neighbor distance as a function of the rank n for the two samples highlighted in figures (a) and (b). The full lines are the log-log linear regressions for the points $n \geq 8$ (see inset figure for a zoomed plot), extrapolated (dashed lines) to $n = 1$, and with corresponding equations in the matching colored boxes. The effective local density is calculated from the linear regression according to Eq. 2.5.

those with which it shares one side of the cell, which we label $1, 2, \dots, \mathcal{N}_i$. The angles are labeled $\alpha_1, \alpha_2, \dots, \alpha_{\mathcal{N}_i}$. Thus for each axon's centroid \mathbf{R}_i we define the quantity

$$\mathcal{Q}_i = \sum_{j=1}^{\mathcal{N}_i} |\alpha_j - \beta|. \quad (2.6)$$

Choosing $\beta = \pi/3$ the comparison is made with a triangular lattice. In this case the PI is also called the hexagonality index (HI) and is defined for each point \mathbf{R}_i by

$$\Delta_i = \frac{1}{\mathcal{Q}_i + 1}. \quad (2.7)$$

It follows that the mean HI is 1 for a perfect triangular lattice, and it approaches 0 as the points deviate more and more from a triangular lattice. (The typical mean HI for random samples is ~ 0.30 .)

In order to study in detail the size of the myelinated axons and their relation with the environment constituted of the other myelinated axons we consider the areas of the axons and the correlation between them, as well as the area of the respective Voronoi cells and the correlations between them. For each axon / Voronoi cell we calculate the average of the areas of the neighboring axon $\langle A'_i \rangle$ / Voronoi cell $\langle \mathcal{A}'_i \rangle$. We plot this against the area of the central axon A_i / cell \mathcal{A}_i under consideration and perform a linear regression. We then repeat the procedure for the second shell of neighbors for which the average area is denoted $\langle A''_i \rangle$ / $\langle \mathcal{A}''_i \rangle$. We define the first shell of neighbors of an axon as the set of axons contained in neighboring Voronoi cells. Similarly, the second shell is defined by the set of axons contained in the neighboring Voronoi cells of the first neighbors themselves.

In addition to the positions of the axons, the shape of their cross sections may also change with age. These morphologic changes may be due to alterations in the myelin sheath [5, 14] or even due to the compression of axons caused by the close packing of neighboring structures. Here we use six shape features to determine whether there

are any differences between myelinated axons in rhesus monkeys with distinct ages. The six features are perimeter, elongation, circularity, diameter, mean curvature, and bending energy as defined in Ref. [77].

2.6 Classification and Feature Selection

Many biological studies use statistical tests to quantify the relevance of a feature. A typical approach is to obtain the probability distributions for the feature in different types of samples and then compare the statistical significance of the difference between their mean. Here we take a different approach. We use the K-nearest neighbors classifier with $K = 3$ to find the accuracy of the measured features when used to classify the samples in either of two classes (i.e., either the young or old class). This approach has the clear advantage that the obtained value can be easily interpreted. For example, an 84% of accuracy for a feature means that in 84% of the cases the feature will correctly identify whether the sample comes from a young or old subject. To perform this task we used the K-nearest neighbors classifier, primarily because it is simple and its interpretation is straightforward in terms of class assignment (i.e., young or old). This classifier also has only one parameter: the number of neighbors. We repeat the analysis for other classifiers and find little variation in the accuracy values obtained using the K-nearest neighbors classifier. The other classifiers used were Naive Bayes, Bayesian Network, Logistic, C4.5, Classification and Regression Tree (CART), and Multilayer Perceptron.

Having measured a given set of features for all the samples, the classification procedure is performed according to the following steps. We first standardize the values for each feature by subtracting their mean and dividing by their standard deviation. We then randomly divide the 67 samples into five different groups (henceforth called *folds*) with the only restriction that each fold has, as far as possible, the same percentage of samples from each class as the complete set. We use the samples contained

in four of the folds to *train* the classifier, i.e., to define the regions in the feature space that should be associated with each class. We next use the fold that was excluded in the training to *validate* the classifier, i.e., we test how many samples in the excluded fold are correctly assigned to the class it originally belongs. For the 3-nearest neighbor classifier, the class assignment is done by determining, for each sample of the excluded fold, the first three neighbor samples belonging to the training folds. We then assign the sample to the class of the majority of these three. We repeat this procedure four more times, each time excluding a different fold from the training in order to use it for validation. In the end we have for each fold the number of samples correctly assigned to its class. This in turn can be represented by a percentage of correctly classified samples, which we designate the accuracy level for the given set of features. This process is called a *stratified cross-validation* and it is the most common approach to estimating the performance of a classifier when the number of samples is small. Finally, because there might be some variation in the accuracy value depending on how the samples were divided, we run the cross-validation procedure five times and take the mean over the five runs. We note that increasing the number of runs does not reduce the variance of the accuracy values found, and this indicates that five runs are sufficient to obtain a reliable accuracy value.

To find the set of features that can best discriminate between the young and old age groups, we employ the feature selection technique [3,4,75,93]. The ideal situation would be to calculate the accuracy for every single set of features and to keep only the set providing the highest accuracy, but because the number of possible sets grows exponentially with the number of features, a heuristic is needed in order to search for the optimal subset. The heuristic we use is the best-first search [83] that starts with the empty set and successively adds the features that provide the largest increase in accuracy. When the search gets stuck in a local optimum, i.e., when there are no more feature additions that can improve the accuracy, it jumps to a previously visited set and adds the feature providing the second-best accuracy found. The search continues

until the number of allowed jumps is attained. In our case we allow 50000 jumps.

Chapter 3

Differences of Myelinated Axons with Age

In this chapter we present our main results regarding the differences observed in EM images between a set of young female subjects and a different set of old female subjects. We quantify these differences and calculate which features are the most changed from one group to the other.

3.1 Recognition and Characterization of Myelinated Axons

In Fig. 3.1 we show a diagram illustrating the steps we take to characterize the myelinated axons from each electron microscope (EM) image. We start with an EM image of the fornix, showing a cross-sectional cut of the myelinated nerve fibers. Using the recognition algorithm described in Section 2.2, we obtain the outlines of the axolemma of myelinated axons. Based on this recognition protocol, we determine, for each myelinated axon, the following properties: the centroid position \mathbf{R}_i , its area A_i , the area of its Voronoi cell \mathcal{A}_i and 6 morphologic features known to provide a good description of a shape's geometrical properties, i.e., perimeter, elongation,

circularity, diameter, mean curvature and bending energy [77]. In Fig. 3.1(a) we see a representative EM image of a young subject, while the recognized axons are shown overlaid on top of the original EM image in Fig. 3.1(b). In Fig. 3.1(c) we draw a schematic diagram of the system in order to clearly visualize the properties used as a basis for our analysis.

Using these 9 individual axon properties as a basis, we derive a collection of different features for each sample (i.e., each EM image). These include statistical moments of the distributions (mean, standard deviation, skewness) as well as correlations between the axon properties. These features can be classified into three categories: macroscopic, morphologic and structural features. Macroscopic features, related to the characteristics of collections of axons, include quantities such as density and the fraction of occupied area (i.e., the ratio of the area occupied by the myelinated axons to the total sample area). Morphologic features refer to characteristics of individual axons and include parameters of the area distribution, perimeter, circularity and curvature, for example. Finally, structural features, related to the relationship between different axons in each sample, include, among others, parameters of the nearest neighbors distributions and quantities derived from the Voronoi analysis such as the mean hexagonality index and the mean number of Voronoi neighbors.

3.2 Single Feature Analysis

We begin our analysis by considering each feature individually, and calculating its mean value for each EM image, or sample. We determine the accuracy of each feature when used to discriminate between 3 young adult subjects and 3 old adult subjects, defined as the cross-validated percentage of correctly classified samples [78] and calculated using a K-nearest neighbors classifier [79], with $K = 3$ (see Section 2.6 for details). We note that accuracy refers to the correct classification of the individual samples, i.e., each EM image, and not of the entire set from each subject. In order

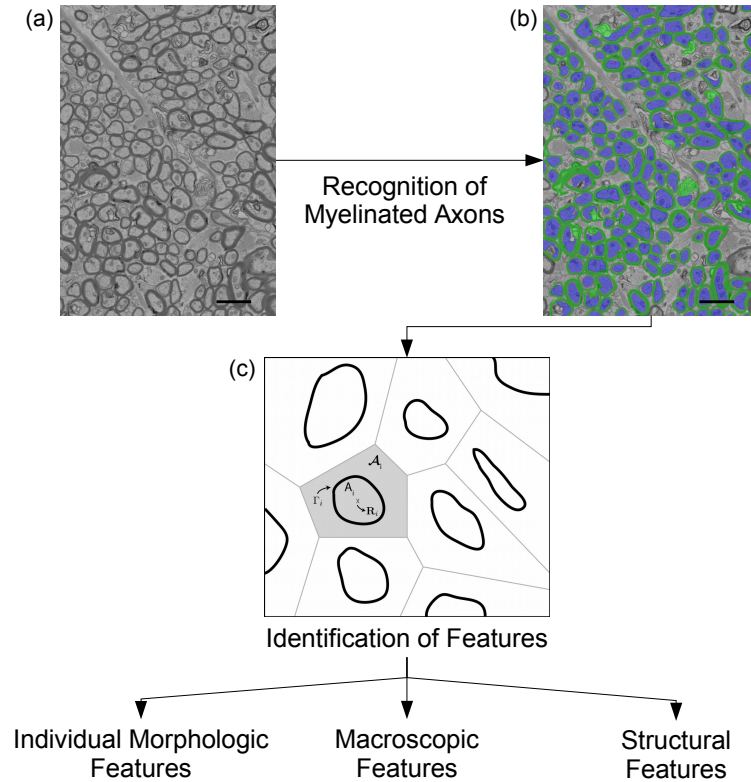


Figure 3.1: Processing steps for characterizing myelinated axons and their structure. The characterization process is done on the EMs of the fornix, belonging to 25 different subjects. (a) We show, as an example, one of the EM images of subject AM077 (6.4 years old). The scale bar (in black) measures $2 \mu m$. (b) Our recognition algorithm (see Section 2.2 for details) is used to segment the areas of myelinated axons (in blue) and the myelin sheath surrounding them (in green). (c) Schematic diagram of a small set of myelinated axon contours and the respective Voronoi tessellation of the embedding space. For one of the axons we show the relevant properties used to characterize each axon: they are the centroid position \mathbf{R}_i , axon area A_i , Voronoi cell area \mathcal{A}_i and axon shape parameters, collectively referred to as Γ_i . These properties are then used as a basis to calculate the features used to describe each EM image (e.g., axon density, hexagonality index, etc.).

to estimate the statistical difference between the two age groups, we also perform for each feature, a Welch's t-test on the mean values for each sample. In Fig. 3.2 we show the estimated probability density functions for 4 representative features, as well as the accuracy (Acc) and the p-value of the Welch's t-test.

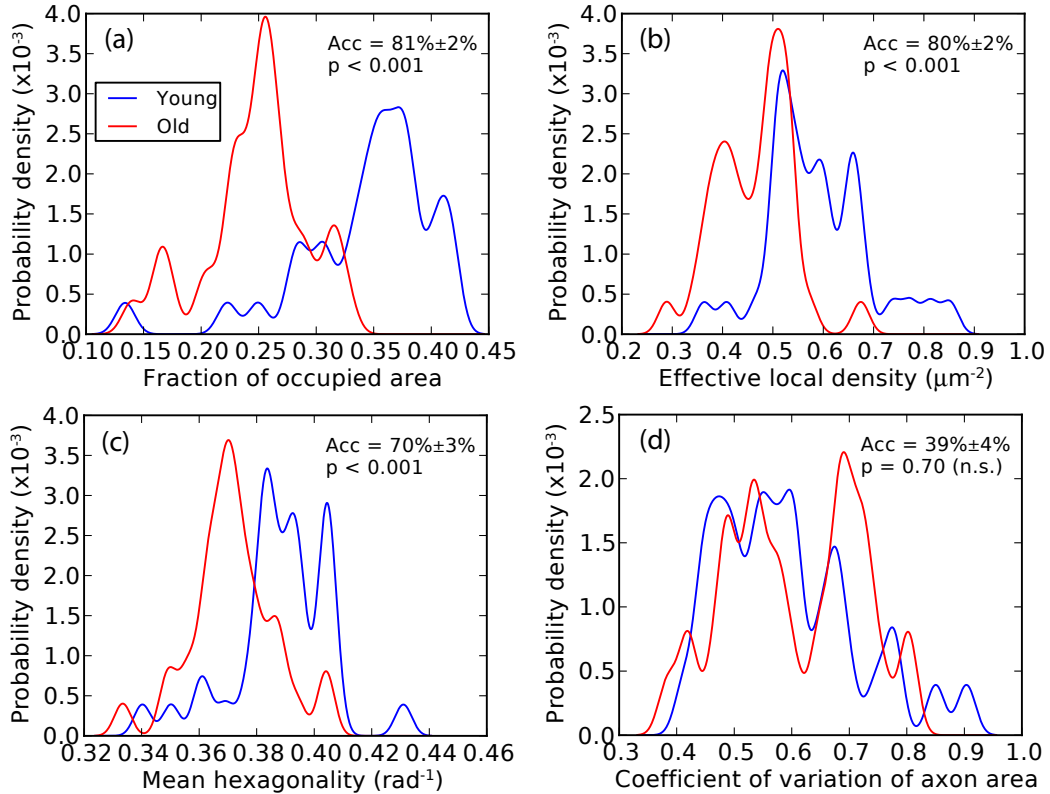


Figure 3.2: Single feature analysis. Probability density functions of 4 representative features for the young group (in blue) and old group (in red). Figures (a) and (b) show the two features providing the highest accuracy in age group classification. Figure (c) shows a feature representative of the system's structural regularity. Figure (d) shows the feature providing the lowest accuracy in age group classification. The probability density functions are determined by using a Gaussian kernel density estimation method. In each plot we also show the accuracy in classification using that single feature, and the Welch's t-test p-value detailing the statistical difference between the two distributions (n.s. stands for not significant, $p > 0.05$).

Fig. 3.2(a) and Fig. 3.2(b) show the two features that provide the best accuracy in classification, i.e., differentiating between membership in the young versus the old

group. Since it is known that myelinated axon density declines with age [5], we expect to obtain high accuracies for density related features. The fraction of occupied area, shown in Fig. 3.2(a), is one such feature. It combines the macroscopic information provided by the density with the morphologic information given by the area of the axons. We find that such combination leads to an 81% accuracy for discrimination between age groups. Another interesting result comes from the effective local density, Fig. 3.2(b). We see that this feature has an accuracy of 80%, which is almost the same accuracy as the fraction of occupied area, and is a better single feature discriminant of the two age groups than the actual axon density, which has an accuracy of 75%.

The effective local density introduced above is defined as the density of a random particle distribution (i.e., a Poisson point process) with the same n -th nearest neighbor distance scaling (see Section 2.5 for definition). By considering only the nearest neighbor distances, the effective local density depends only on how closely packed the axons are, thus providing an estimate of the local density around the axons, ignoring the presence of any abnormally large axon-free regions occupied by excessive myelin sheath or other biological elements such as glia and blood vessels. We define an axon-free region as any region in the EM image that is not occupied by a myelinated axon. Samples with a higher effective local density compared to the actual axon density have regions with large clustered axon-free areas with no myelinated axons, that skew the axon density measurement towards smaller values. On the other hand, samples with lower effective local density compared to the axon density have its axon-free regions spread out, i.e., equally distributed throughout the sample, with little to no clustering effect.

We observe that the axons have different structures in the two age groups, reflected in the difference of the hexagonality index, shown in Fig. 3.2(c). The hexagonality index measures the angular regularity of a structure, and is equal to 1 when the system is perfectly ordered as a triangular lattice, decreasing in value as a system's disorder increases [80] (see Section 2.5 for definition). From Fig. 3.2(c), we see that samples

from the old subjects have a lower hexagonality index than the young subjects, reflecting an increase in disorder with age. Despite the observable increase in disorder with age, we find that the mean number of neighbors, measured by the number of adjacent Voronoi cells, is the same for both the young and old age groups: 5.93.

Finally, Fig. 3.2(d) shows the feature that gives the worst accuracy: the coefficient of variation of the axon area, a morphologic feature. In fact, considering the rest of the morphologic features, most provided low accuracies and showed no significant differences between the two age groups. In other words, there is no observable change in axon size or axon shape with aging, with the mean elongation being the only exception, with an accuracy of 61%.

3.3 Feature Selection

Using single features, the highest accuracy attained distinguishing between samples from young and old is 81%. When all features are considered together the accuracy increases only to 84%, just a slight increase from the single feature case with the highest accuracy. This reflects the fact that using a high dimensional space of features comes with many issues for classification (e.g., difficulty in sampling entire space, increased execution time, additional classification noise) [81], especially when there are many irrelevant features.

To reduce the dimensionality of the fornix data and avoid problems associated with the high dimensionality one could consider using the Principal Component Analysis (PCA) procedure [82] to reduce the dimensions of the data to a few components that account for as much variability in the data as possible. However, since we are not interested in describing the variability of the age groups but in distinguishing between them and pinpointing which features are the most important for that task, we used an alternative technique called feature selection [3, 75]. This technique aims to find a subset of features that, *when combined*, gives a good separation between classes (i.e.,

the two age groups). In this technique, one considers a subset of features instead of each one individually, since features that alone do not give a good separation between classes can significantly improve discrimination when combined with other features [3, 75]. In a similar fashion, two highly correlated features, which in principle would hold redundant information, can also help the discrimination process in some cases.

3.4 Two Feature Analysis

Although the feature selection technique does not fix the size of the subset of features *a priori*, for reasons that will be clear below, we start by limiting the subset size to 2. From the total of 990 possible pairs of features, we keep only those pairs with more than 85% of accuracy. The fraction of occupied area makes connections with many other features (usually called a hub in network terminology), which confirms the importance of this feature. Considering that the fraction of occupied area alone already provides an accuracy of 81%, it is expected that a small contribution to the classification from another feature will create a link between the two features. However, this high connectivity is not replicated by other features with similarly large accuracies (e.g., effective local density, third nearest neighbor mean distance).

The highest accuracy for the age group separation is achieved for the combination of fraction of occupied area and effective local density, with a 90% accuracy. However, considering that the change of the class of a single sample roughly translates to a 1.5% difference in accuracy, other pairs of features with small differences in accuracy should also be taken into consideration. In fact, the pairs of features that result in the highest accuracies are: the combination of the fraction of occupied area (macroscopic feature) with either the effective local density or the hexagonality index (structural features); or the combination of the mean perimeter (morphologic feature) with either the second nearest neighbor mean distance or the third nearest neighbor

mean distance (structural features). These 4 pairs of features result in accuracies larger than 87.5% in the age group separation. We note that the fraction of occupied area is strongly correlated with structural features such as mean hexagonality index and effective local density, which means that these feature combinations bring some redundant information to the classification. Despite this redundancy, there is still a significant improvement in the sample separation accuracy when combining the fraction of occupied area with the effective local density or the mean hexagonality index.

3.5 Multiple Feature Analysis

In order to determine if the age group separation can be improved by considering larger subsets of features, we perform the same calculations for subsets of three features. We note that the maximum obtained accuracy value is 91%, compared to 90% for the pairwise case, which means that little information is added when including a third feature. In fact, considering the pairs of features that result in the highest accuracies, the inclusion of another degree of freedom in the classification procedure, in the form of an additional feature, would only correct, at best, one misclassified sample. Since including one degree of freedom only to correctly classify one more sample does not provide much benefit to the procedure, the addition of a third feature is unnecessary.

Removing the limit imposed on the subset size, we use feature selection to search for the highest possible classification accuracy that one can achieve for any subset of features. Since the number of possible subsets is large, we use a best-first search algorithm [83] to search for the best subset considering all possible combinations of features (see Section 2.6 for details). We find that the highest accuracy we can achieve is 94%, for a subset containing 6 features (the features in the subset are: `FracOccupArea`, `EffDensity`, `PearsonR1stShellAxon`, `Skewness2ndNNDist`,

Skewness3rdNNDist and StdDevElongation). Although this subset represents a small increase from the 90% maximum accuracy we obtain for pairs of features, we note that the extra 4 features only helped correct, at most, 3 misclassified samples. Therefore, we conclude that the best approach to characterize the aging of the rhesus monkey fornix is to consider the fornix samples in a 2D space, where the samples are characterized by pairs of features.

3.6 Best Age Discriminant

When considering the two feature analysis, several pairs of features provide a high classification accuracy. In fact, four pairs of features result in accuracies larger than 87.5% in the age group separation. In order to choose the pair more pertinent to the age group separation, we measure the scatter distance between the two classes [84], revealing the difference in the mean distance between classes for pairs of features with similar resulting accuracies. Thus, we look for a pair of features that provides both a high accuracy in the age group separation as well as a large distance between the classes. Following this criterion, the most relevant pair is formed by the fraction of occupied area and the effective local density. In Fig. 3.3 we show a scatter plot of the fornix samples in the 2D space formed by these two features, where we see that the young and old groups are well separated, with only 6 samples falling in the wrong age class.

We note that, similarly to what is revealed in the single feature analysis, the combination of effective local density and fraction of occupied area, which has an accuracy of 90%, provides a better discrimination than the pair formed by the axon density and fraction of occupied area, which has an accuracy of only 81%. In fact, by replacing axon density with effective local density, a fraction of the misclassified samples migrate to their respective age group. Although these results were obtained using the K-nearest neighbors classifier, when considering other algorithms for classifica-

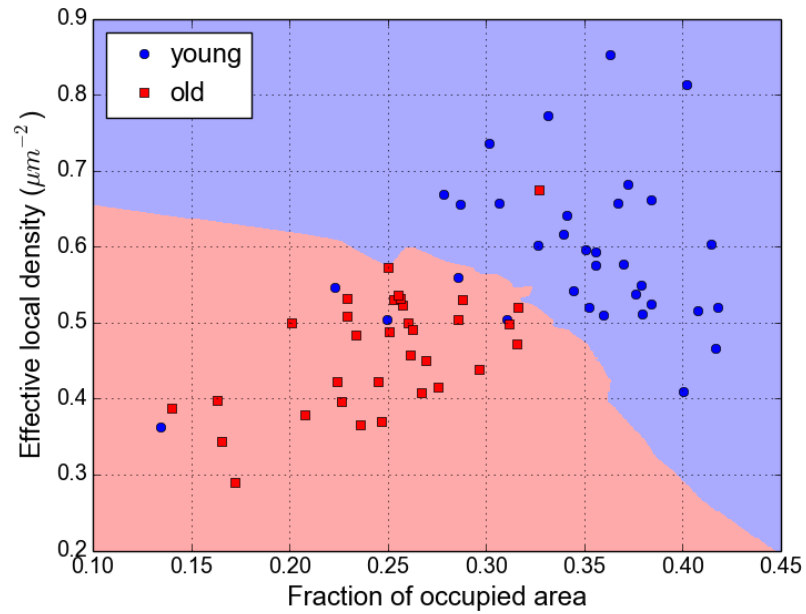


Figure 3.3: Locations of the fornix samples in a two features space. At the center we show the scatter plot of all samples belonging to the 6 different subjects, depending on their fraction of occupied area and effective local density. Samples belonging to the young subjects are represented in blue while samples of the old subjects are in red. These two features not only provide a good accuracy for age group discrimination, but also have a relatively large class scatter distance.

tion, we observe that the combination of fraction of occupied area and effective local density commonly appears as one of the most accurate pair of features, validating our results (the other classifiers used were: Naive Bayes, Bayesian Network, Logistic, C4.5, Classification And Regression Tree - CART and Multilayer Perceptron).

Chapter 4

Effects of Aging and Sex on the Myelinated Axons

In this chapter we present our main results for both the individual properties and the macroscopic properties of the myelinated axons in the fornix. We describe these results and explain how they are affected by the aging process. We also measure how the different cognitive profiles of the different subjects are affected might be affected by the myelinated axons properties.

4.1 Density Properties of Myelinated Axons

4.1.1 Dependence on age

Previous studies have demonstrated that the myelinated axon density declines with age [5, 10]. In our analysis, we calculated the density of the recognized myelinated axons and plotted them against the age of the subjects, as seen in Fig. 4.1. Looking at our data, we confirm that the myelinated axon density has a statistically significant decrease with age, as shown by the linear regression with $p = 6.5 \times 10^{-6}$. This decrease remains significant when separating the subjects by sex, as shown in Fig. 4.2.

Despite both sexes presenting a decrease of myelinated axon density with age,

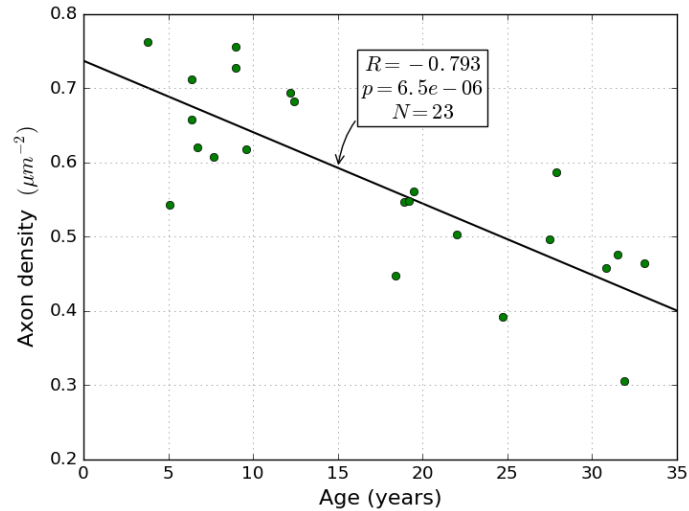


Figure 4.1: Density of the myelinated axons in function of the age of the 23 subjects analyzed. The linear regression is drawn in a solid line, with corresponding Pearson correlation coefficient and p-value.

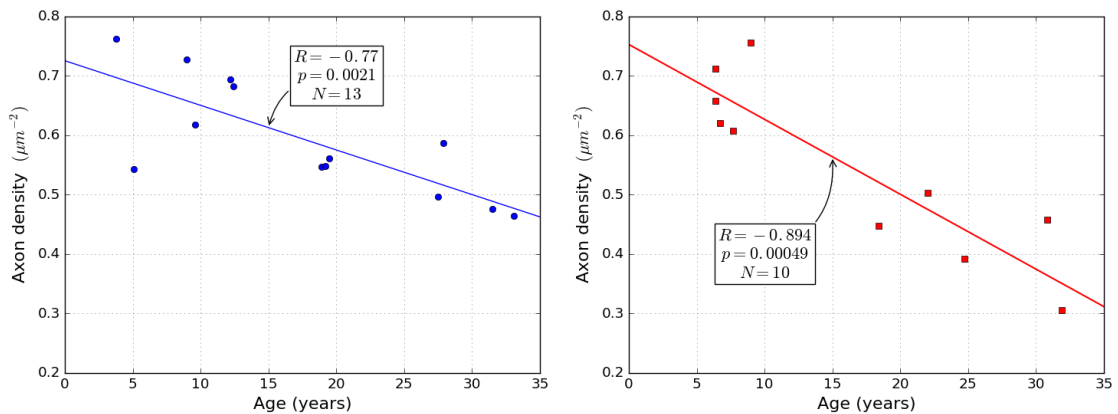


Figure 4.2: Density of the myelinated axons in function of age, for only the male subjects (left) or only the female subjects (right). The linear regression for the male (female) subjects is shown in a solid blue (red) line, with corresponding Pearson correlation coefficients and p-values.

we notice that there's a difference in the density values of older subjects between males and females. In Fig. 4.3, we compare the myelinated axon density between the male and female subjects, after separating them into the 2 age groups: young and old. The young subjects of both sexes have the same average myelinated axon density. However, the female subjects have a lower myelinated axon density than the male subjects for the old group ($p = 0.023$ for a two-sided Mann–Whitney U test). This implies that as female subjects get older, they lose a higher percentage of the myelinated axons in the fornix than their male counterparts.

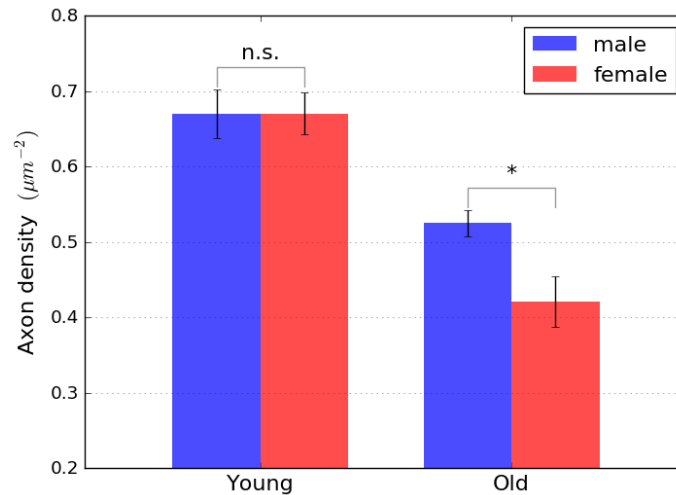


Figure 4.3: Density of the myelinated axons for the 2 age groups, stratified by sex. For each age group, a two-sided Mann–Whitney U test was performed on the density values of all male and female subjects in that age group. In this figure, n.s. stands for not significant. There is a statistical significant difference in the density values between the old males and old females ($p = 0.023$).

The cross-sectional areas of the fornix of the subjects used in this study were previously measured in Ref. [5], where it was shown there was no correlation between the area of the fornix and age. Even when we separate the subjects by sex, no correlation is found. Taking the values of the cross-sectional areas of the fornix from Ref. [5], and the values we measure for the myelinated axon density, we calculate the total number of myelinated axons in the fornix and plot them in function of the age of

the subjects, as shown in Fig. 4.4. The number of myelinated axons for each subject ranges from 6×10^5 to 2×10^6 , and has a significant decrease with age ($p = 1.6 \times 10^{-3}$).

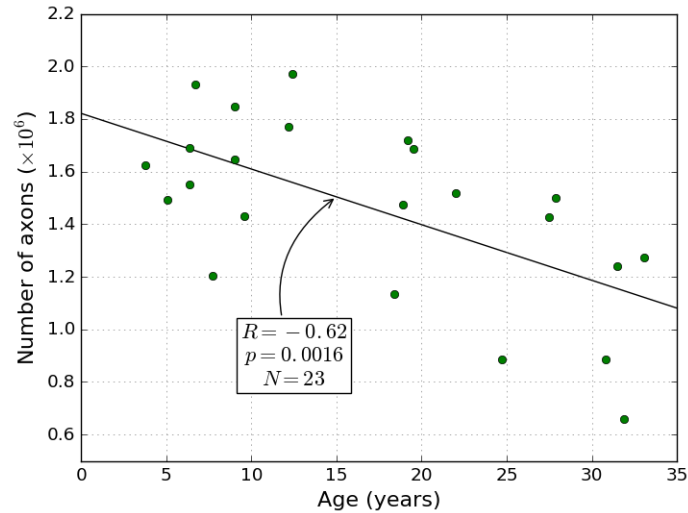


Figure 4.4: Number of myelinated axons in function of the age of the 23 subjects analyzed. The linear regression is drawn in a solid line, with corresponding Pearson correlation coefficient and p-value.

Separating by sex, this decrease in the total number of myelinated axons is still significant for both male and female subjects, as illustrated in Fig. 4.5.

If we consider the 2 age groups separately, as shown in Fig. 4.6, we notice that the young male and young female subjects have similar values for the total number of myelinated axons. However, the female old subjects have a lower total number of axons than their male counterparts. Old female subjects have an average of 1.02×10^6 total myelinated axons while the old male subjects have an average of 1.47×10^6 . Taking a one-sided Mann–Whitney U test, the old female subjects have a significant lower value of total myelinated axons than their male counterparts ($p = 0.026$). Therefore, there is a greater loss in numbers of myelinated axons for female subjects.

In a similar fashion to the myelinated axon density, the fraction of occupied axon area, i.e., the ratio of the total cross-section area of the myelinated axons to the total image area, also displays a significant decrease with age ($p = 3.8 \times 10^{-5}$), as previously

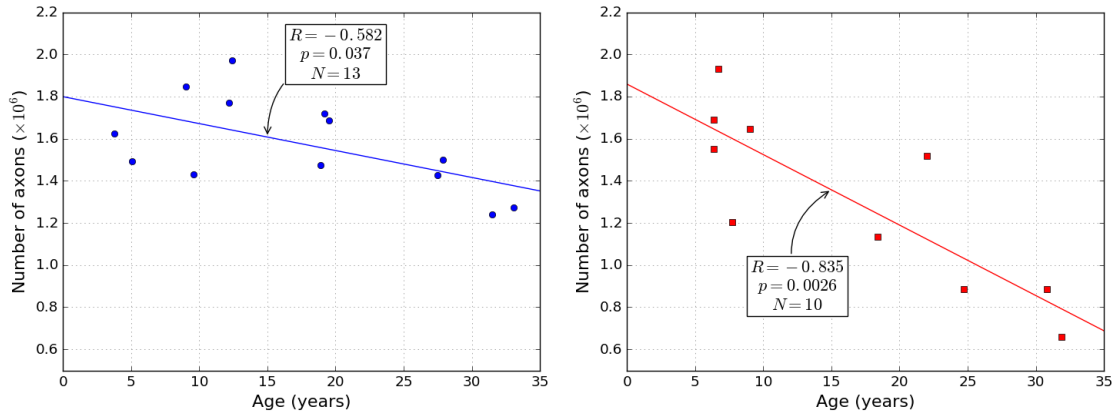


Figure 4.5: Number of myelinated axons in function of age, for only the male subjects (left) or only the female subjects (right). The linear regression for the male (female) subjects is shown in a solid blue (red) line, with corresponding Pearson correlation coefficients and p-values.

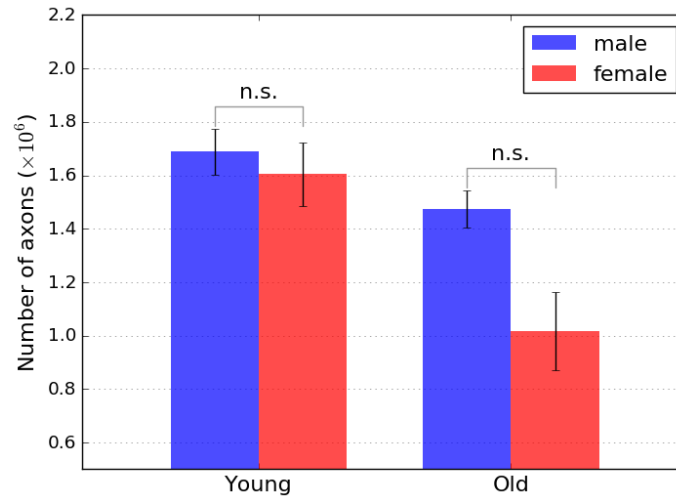


Figure 4.6: Number of myelinated axons for the 2 age groups, stratified by sex. For each age group, a two-sided Mann–Whitney U test was performed on the number of axons of all male and female subjects in that age group. In this figure, n.s. stands for not significant.

shown in Ref. [10]. When separating the subjects by sex, the decrease of the fraction of occupied axon area with age is still observed, although it is more significant for female subjects, as illustrated in Fig. 4.7.

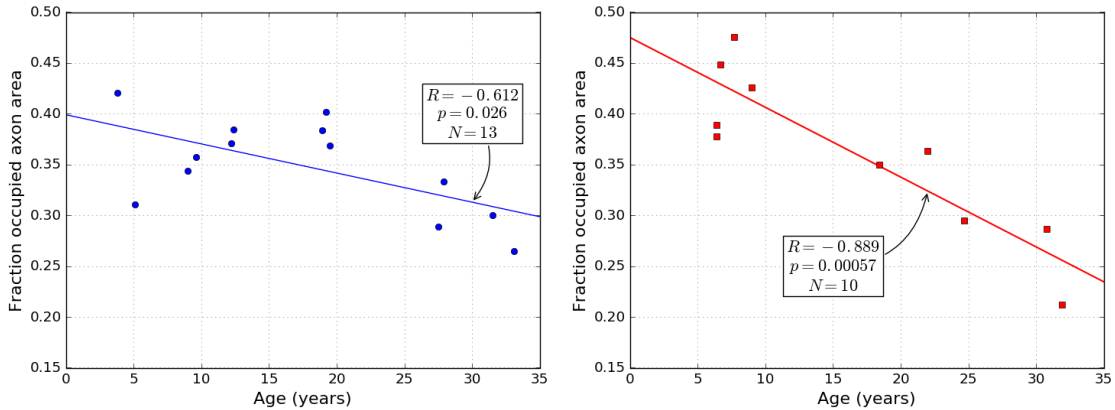


Figure 4.7: Fraction of occupied axon area in function of age, for only the male subjects (left) or only the female subjects (right). The linear regression for the male (female) subjects is shown in a solid blue (red) line, with corresponding Pearson correlation coefficients and p-values.

For each of the 2 age groups, we compare the values of fraction of occupied axon area between the male and female subjects, shown in Fig. 4.8. Contrary to the analysis regarding the density of myelinated axons, we notice that the young females have a higher fraction of occupied axon area than their male counterparts ($p = 0.018$ for a one-sided Mann Whitney U test), while having the same myelinated axon density. However, there is no statistical difference between the values of the fraction of occupied axon areas of the old male and old female subjects.

Considering both the fraction of occupied axon area and myelinated axon density values, we can say that the young female subjects have higher fraction of occupied axon area values than the young male subjects, while having the same myelinated axon density. This would imply that young female subjects have a larger average axon area than the young male subjects. For the old group, the old female subjects have similar values of fraction of occupied axon area than the old male subjects, while having lower myelinated axon density values. Once again, this fact implies a higher

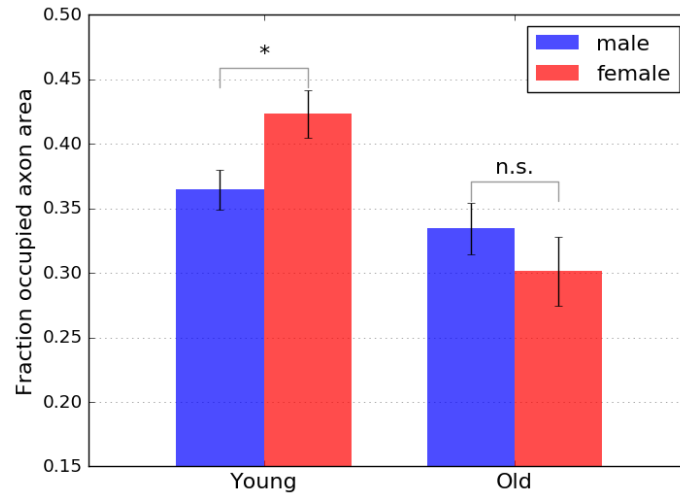


Figure 4.8: Fraction of occupied axon area for the 2 age groups, stratified by sex. For each age group, a two-sided Mann–Whitney U test was performed on the fraction of occupied axon area values of all male and female subjects in that age group. In this figure, n.s. stands for not significant. There is a statistical difference in the fraction of occupied axon area values between the young males and young females ($p = 0.036$).

average axon area for the old female subjects as well. In fact, female subjects must have a higher average axon area than their male subjects for both age groups.

We also calculate the fraction of occupied fiber area, i.e., the ratio of the total cross-section area of the myelinated axons plus the surrounding myelin sheath area to the total image area. As was the case for the fraction of occupied axon area, the fraction of occupied fiber area also decreases with age ($p = 4.0 \times 10^{-5}$). The same decrease with age is observed when separating the subjects by sex, as shown in Fig. 4.9.

When comparing the male and female subjects for each of the 2 age groups, shown in Fig. 4.10, we detect no statistical difference between the 2 sexes. As such, for each age group, there is no sex difference in the fraction of space not occupied by either the axons or their myelin sheath, which would imply similar structural packing properties between the male and female subjects.

Another point raised by the sex difference observed for the fraction of occupied

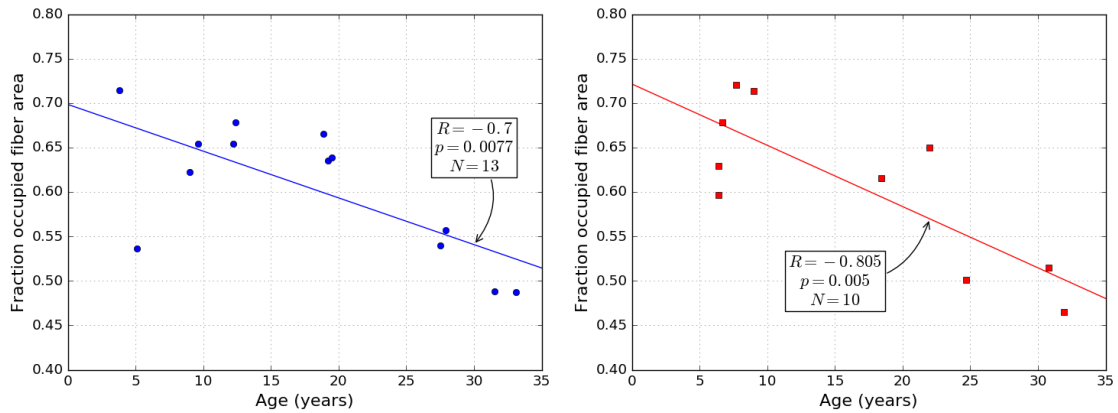


Figure 4.9: Fraction of occupied fiber area in function of age, for only the male subjects (left) or only the female subjects (right). The linear regression for the male (female) subjects is shown in a solid blue (red) line, with corresponding Pearson correlation coefficients and p-values.

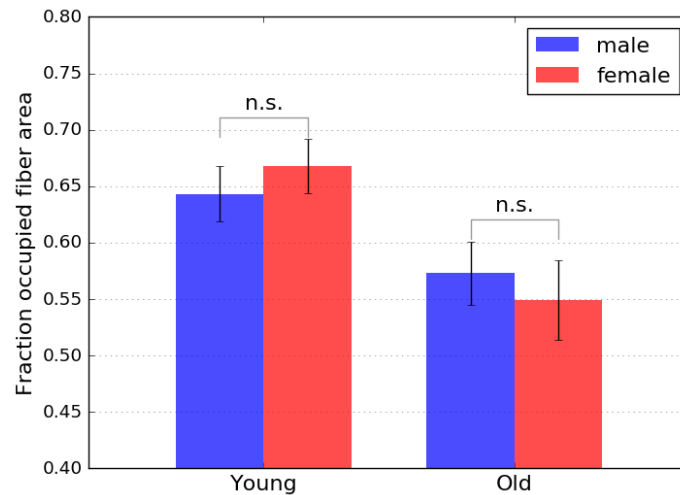


Figure 4.10: Fraction of occupied fiber area for the 2 age groups, stratified by sex. For each age group, a two-sided Mann–Whitney U test was performed on the fraction of occupied fiber area values of all male and female subjects in that age group. In this figure, n.s. stands for not significant.

axon area in the young group and the lack of a difference for the fraction of occupied fiber area is the smaller fraction of space occupied by myelin sheath for young female subjects, when compared to the male subjects of the same age group.

4.1.2 Dependence on cognitive profile

Instead of considering the dependence of the axon properties on the age of the subjects, we analyze the correlation of the axon properties with the cognitive profile of the subjects, in order to assess if any of the measured axon properties could have influenced the cognitive skills of the subjects. The cognitive profile of each subject was measured by the cognitive impairment index (CII), introduced in Ref. [9].

There is an observed correlation between the myelinated axon density and the CII values of the subjects ($p = 0.013$), although with a lower significance compared to the age dependence of the myelinated axon density. When separating by sex, the correlation of the myelinated axon density with the CII is not statistically significant.

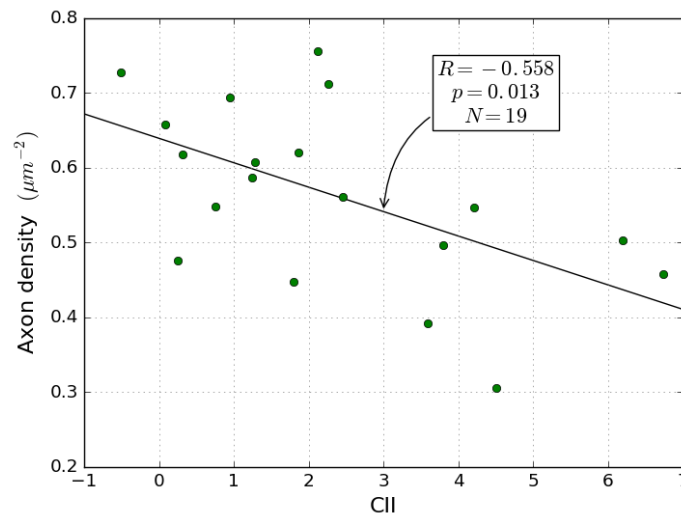


Figure 4.11: Myelinated axon density in function of the CII of the 23 subjects analyzed. The Pearson correlation coefficient and p-value for all subjects is shown in the figure. Separating by sex, the Pearson correlation coefficient for the male subjects is $R = -0.50$ with $p = 0.17$ ($N = 9$), while for the female group we get $R = -0.57$ with $p = 0.087$ ($N = 10$).

Both the fraction of the occupied axon area and the fraction of occupied fiber area display no statistical correlation with the CII of the subjects, either when considering all the subjects or when separating them by sex.

4.2 Axon Areas

4.2.1 Distribution of axon areas

Another advantage of the myelinated recognition algorithm, compared to previous studies [5, 8, 17], is that it not only gets the positions of the myelinated axons, but also their shape properties (e.g., their cross-section area). Using the data gathered by the recognition algorithm, we calculated the cross-section areas of all myelinated axons for all subjects. These areas were calculated from the points that define the contour of each axon. Given a set of discrete contour points (x_i, y_i) ordered sequentially $i = 1, \dots, n$ in the plane, the area of the polygon limited by these contour points is given by [16, 18]

$$A = \frac{1}{2} \sum_{i=1}^n x_i y_{i+1} - x_{i+1} y_i, \quad (4.1)$$

where $x_{n+1} = x_1$ obeys a periodic boundary condition.

With that information, we plotted the distribution of axon areas for each subject, as shown in Fig. 4.12. We notice that each subject's axon area distribution follows a log-normal distribution, characterized by the following probability density function

$$f(x) = \frac{1}{x\sigma\sqrt{2\pi}} \exp - \frac{(\log x - \mu)^2}{2\sigma^2}, \quad (4.2)$$

where μ and σ are the parameters of the distribution. Note that the log-normal distribution is equivalent to the normal distribution of $\log x$, with mean μ and standard deviation σ .

The normality of the log of the axon areas can be confirmed analytically via an Anderson-Darling test, a normality test used to determine if a data set is well modeled

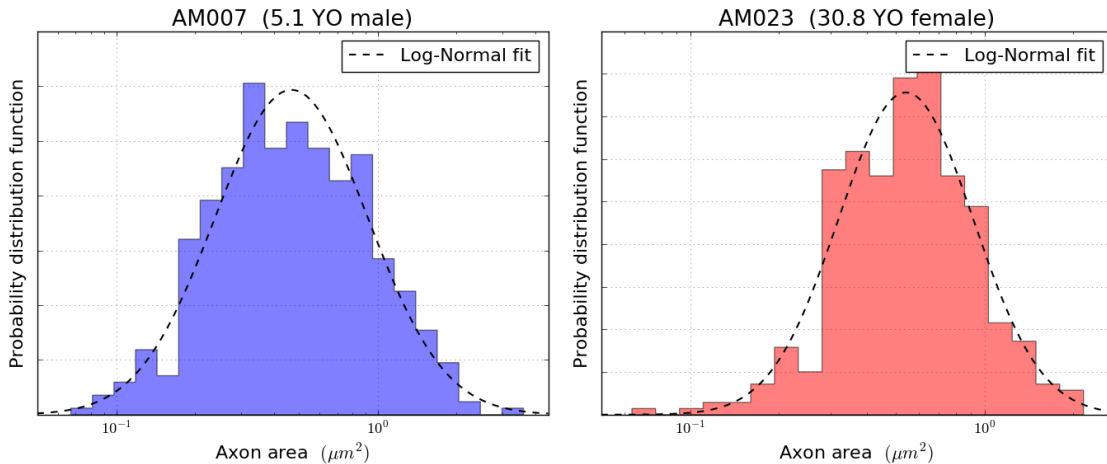


Figure 4.12: Histogram of the probability distribution function of the myelinated axon areas for 2 particular subjects. On the left in blue, is shown the axon area distribution of AM007, a young male subject, while on the right in red is the axon area distribution of AM023, an old female subject. Note that the scale of the x-axis is logarithmic. For each subject, we fit a log-normal distribution to the data, shown as a dashed line. For both subjects, we performed an Anderson-Darling test for normality of the $\log(\text{area})$ data. For subject AM007, we get $p = 0.28$ for $N = 444$, while for subject AM023, we have $p = 0.27$ for $N = 374$.

by a normal distribution. In the 2 cases shown in Fig. 4.12, the Anderson-Darling test says we can't reject the null hypothesis of $\log(\text{area})$ coming from a normal distribution with $p = 0.28$ for AM007, and $p = 0.27$ for AM023.

A log-normal distribution has been observed for other biological systems [19, 20], e.g., the size of senile plaques in Alzheimer's disease. This behavior can be explained via a model of stochastic geometric growth, or geometric Brownian motion. In this model, each unit of a system experiences a random growth, in which its average is proportional to the unit's size. This is equivalent to the Gibrat's law of proportionate growth, defined initially to model firm sizes. In simple terms, this geometric growth can be modeled as a discrete multiplicative process, where the axon area at time $t_n = n\Delta t$ (A_n) follows the recursive equation $A_{n+1} = X_n A_n$, where X_n is the growth rate at time t_n . The growth rates defined by the set $\{X_n\}_{n=0,1,\dots}$ are independent identically distributed random variables. At a time t_n , with $n \gg 1$, the axon areas

are given by

$$\begin{aligned} A_n &= \prod_{i=0}^{n-1} X_i A_0 \\ \log A_n &= \sum_{i=0}^{n-1} \log X_i + \log A_0 . \end{aligned} \quad (4.3)$$

Considering X is a random variable, so is its logarithm $Y = \log X$ and, by the central limit theorem, its sum tends towards a normal distribution. As such, the logarithm of the axon areas tends towards a normal distribution, more concretely

$$\log A_n \sim \mathcal{N}(n\mu_Y + \log A_0, n\sigma_Y^2) , \quad (4.4)$$

where μ_Y and σ_Y^2 are the mean and variance of the random variable $Y = \log X$ and $\mathcal{N}(\mu, \sigma^2)$ is the normal distribution with mean μ and variance σ^2 . Through this model, one could explain why the axon areas display a log-normal distribution.

We also observe that the log-normal distribution fitted to the axon areas has different parameters for different subjects. This indicates that, despite being modeled by the same distribution, there is a biological variability between different subjects, even when they belong to the same age group and sex.

4.2.2 Dependence on age

In order to quantify the influence of aging on the axon areas, we need to first define the characteristic axon area for each subject. Considering that the axon areas follow a log-normal distribution, instead of calculating the average of the axon areas, it is more appropriate to calculate its geometric mean, also called log-average. The geometric mean μ_g of a data set x_i with $i = 1, \dots, n$ is defined by

$$\mu_g = \left(\prod_{i=1}^n x_i \right)^{\frac{1}{n}} . \quad (4.5)$$

Considering that the axon area distribution is a heavy-tailed distribution, where the probability of axons with larger than expected areas is not bounded exponentially, the geometric mean presents the advantage of being less influenced by these axons with larger than expected areas than the simple arithmetic mean. This is the case, since the geometric mean averages the logarithms of the areas, instead of their actual values. In fact, the logarithm of the geometric mean, as shown in Eq. (4.6) is simply the arithmetic mean of the logarithm of the values x_i , hence its name log-average.

$$\begin{aligned}\log \mu_g &= \frac{1}{n} \left(\sum_{i=1}^n \log x_i \right) \\ &= \langle \log x \rangle .\end{aligned}\tag{4.6}$$

We also note that the geometric mean μ_g is an unbiased estimator of the parameter μ of the log-normal distribution, shown in Eq. (4.2). Taking the average for all subjects, we calculate that the average geometric mean of the axon areas is $0.544 \mu m^2$.

In Fig. 4.13, we plot the geometric means of the axon areas for each subject in function of the subject's age, stratified by sex. As is shown, there is no statistically significant correlation between the axon areas and the age of the subject, even when separating by sex. In other words, the typical axon area is not affected by age.

We note that female subjects have slightly higher values for the geometric means of axon areas, as hinted previously by the analysis of the fraction of occupied axon area and myelinated axon density for different age groups. In fact, performing a one-sided Mann–Whitney U test, we can say that the average of the geometric means of the axon areas for the female subjects is larger than the corresponding value for the male subjects ($p = 0.019$). However, when taking each age group individually, the observed sex difference is not considered significant, as shown in Fig. 4.14.

We also study the dispersion of the axon areas distribution in function of age, to determine if there's any increased or decreased variation of the typical axon area for subjects of different ages. In a similar fashion to the geometric mean, instead

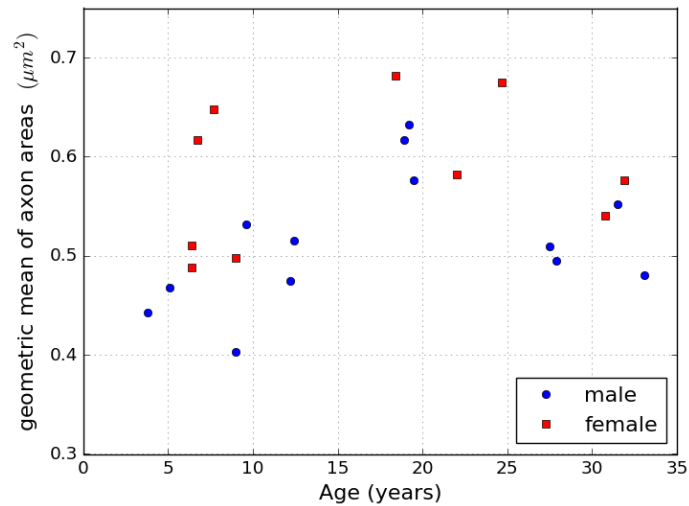


Figure 4.13: Geometric means of the axon areas in function of age, stratified by sex. The Pearson correlation coefficient for all subjects is $R = 0.24$ with $p = 0.27$ ($N = 23$). The Pearson correlation coefficient for the male subjects is $R = 0.35$ with $p = 0.24$ ($N = 13$), while for the female group we get $R = 0.24$ with $p = 0.50$ ($N = 10$).

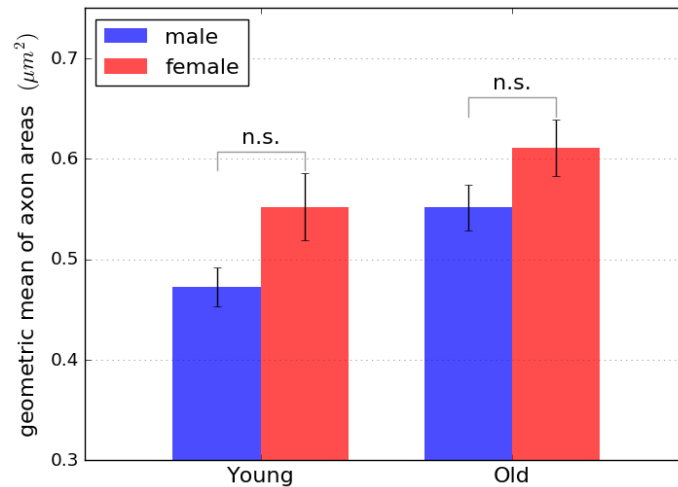


Figure 4.14: Geometric means of the axon areas for the 2 age groups, stratified by sex. For each age group, a two-sided Mann–Whitney U test was performed on the values of the geometric means of the axon areas of all male and female subjects in that age group. In this figure, n.s. stands for not significant.

of calculating the standard deviation of the axon area distribution, we calculate the geometric standard deviation σ_g , defined by the equation

$$\begin{aligned} \log \sigma_g &= \sqrt{\frac{\sum_{i=1}^n \left(\log \frac{x_i}{\mu_g} \right)^2}{n}} \\ &= \sigma_{\log x} , \end{aligned} \tag{4.7}$$

where $\sigma_{\log x}$ represents the standard deviation of the logarithm of the axon area values x . Note that the geometric standard deviation is dimensionless, since it is simply a multiplicative factor.

According to Fig. 4.15, the values of the geometric standard deviation of the axon areas have no correlation with age, even when separating the subjects by sex, just like the case with the geometric means.

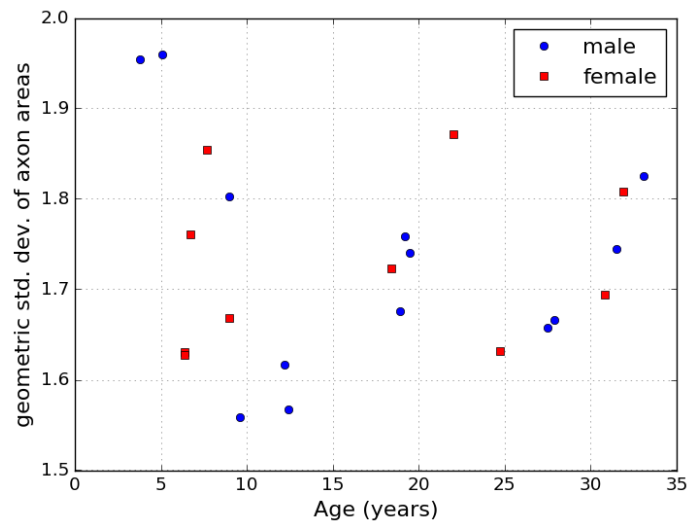


Figure 4.15: Geometric standard deviation of the axon areas in function of age, stratified by sex. The Pearson correlation coefficient for all subjects is $R = -0.069$ with $p = 0.76$ ($N = 23$). The Pearson correlation coefficient for the male subjects is $R = -0.23$ with $p = 0.46$ ($N = 13$), while for the female group we get $R = 0.20$ with $p = 0.58$ ($N = 10$).

Separating by age group, as illustrated in Fig. 4.16, we also do not observe any

difference between the male and female subjects. In fact, all age groups have similar values of the geometric standard deviation of the axon areas, close to the average value of 1.73 for all subjects.

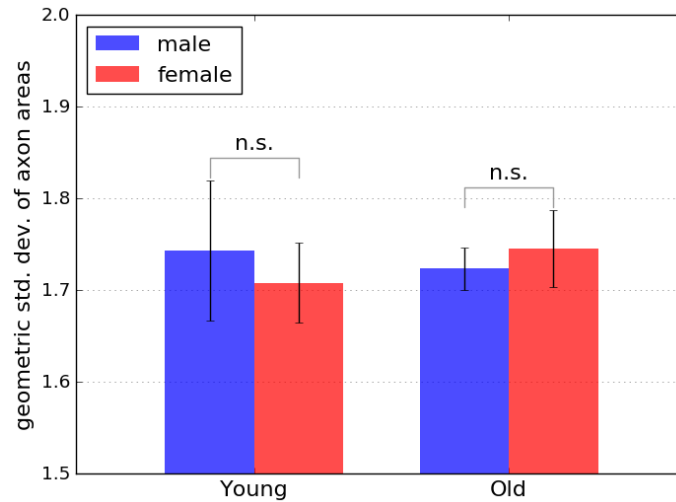


Figure 4.16: Geometric standard deviation of the axon areas for the 2 age groups, stratified by sex. For each age group, a two-sided Mann–Whitney U test was performed on the geometric standard deviation values of all male and female subjects in that age group. In this figure, n.s. stands for not significant.

Considering that the axon area distribution parameters do not change with age, we can say that the young subjects and the old subjects have similar axon area distributions. Therefore, the loss of myelinated axons shown previously is not influenced by the axon areas. In other words, myelinated axons of different sizes are lost at similar rates, thus not changing the axon area distribution.

4.2.3 Dependence on cognitive profile

We also considered the correlation of the axon areas and its dispersion with the CII of the subjects, instead of their ages. As shown in Fig. 4.17, there is no statistical correlation between the geometric means and the CII, even when separating the subjects by sex. The same applies to the geometric standard deviations of the axon areas.

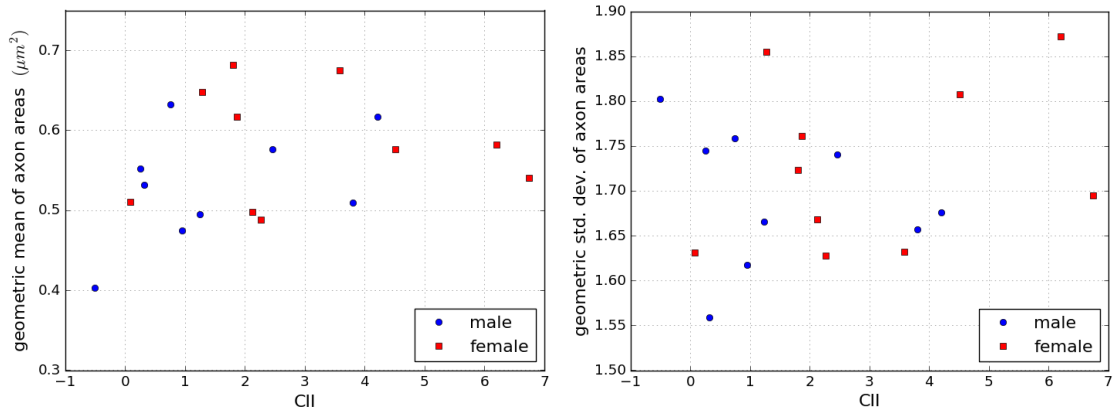


Figure 4.17: Left: Geometric means of the axon areas in function of CII, stratified by sex. Right: Geometric standard deviations of the axon areas in function of CII, stratified by sex. Both reveal no significant correlation with the CII of the subjects.

In conclusion, the axon areas are not affected by the age of the subjects and show no correlation with their cognitive profile.

4.3 Myelin Sheath Properties

Since our recognition algorithm has the added functionality of recognizing the myelin sheath surrounding the myelinated axons, we are able to measure quantities related to the myelin sheath, such as its thickness or its correlation with the surrounded axon, measured via the g-ratio of the myelinated axon, i.e., the ratio of the axon diameter to the fiber diameter (axon+myelin). With the myelin sheath data from more than 10,000 myelinated axons, we performed an analysis of the association of these parameters with age.

Note that the outer myelin detection algorithm ignores large localized deviations of the myelin sheath thickness around each axon, as they typically arise from biological myelin degeneration or from tissue processing defects. Therefore, any localized myelin defects do not influence the measured individual morphological properties, as is the case of the myelin thickness and the g-ratio.

4.3.1 Mean myelin thickness

We start by analyzing the myelin sheath properties of the myelinated axons by calculating the mean myelin thickness for each axon and determining its average value for each subject. The myelin sheath thickness is calculated for each point of the recognized contour of the axon, i.e., the axolemma. From the distribution of the myelin sheath thickness along each axon's contour, we calculate its mean value as well as its standard deviation per axon. The average of the mean myelin thickness values for all subjects is $0.130\mu m$.

In Fig. 4.18, we plot the average of the mean myelin thickness values against the subject's age and observe an increase in the mean myelin thickness with age ($p = 3.4 \times 10^{-3}$). This statistically significant increase of the mean myelin thickness with age occurs despite the absence of any correlation of the average axon area with age, as shown in Fig. 4.13, and previously reported in Ref. [10]. In other words, we observe a generalized increase of the myelin thickness with age while the axons display no change in their areas.

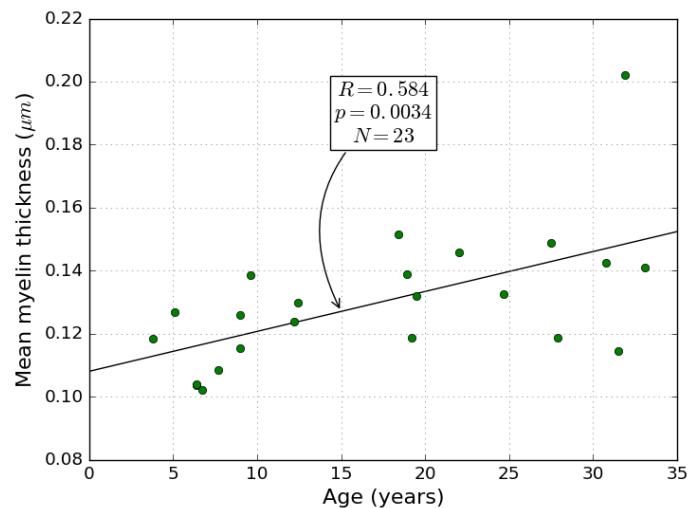


Figure 4.18: Average of the mean myelin thickness values of the myelinated axons in function of age for the 23 subjects analyzed. The calculated linear regression is shown in a solid line, with corresponding Pearson correlation coefficients and p-values.

However, when separating the subjects by sex, we notice that this correlation is only present on the female subjects, as illustrated in Fig. 4.19. While there is a statistically significant increase of the mean myelin thickness with age for the female subjects ($p = 1.3 \times 10^{-3}$), there is no correlation observed for the male group.

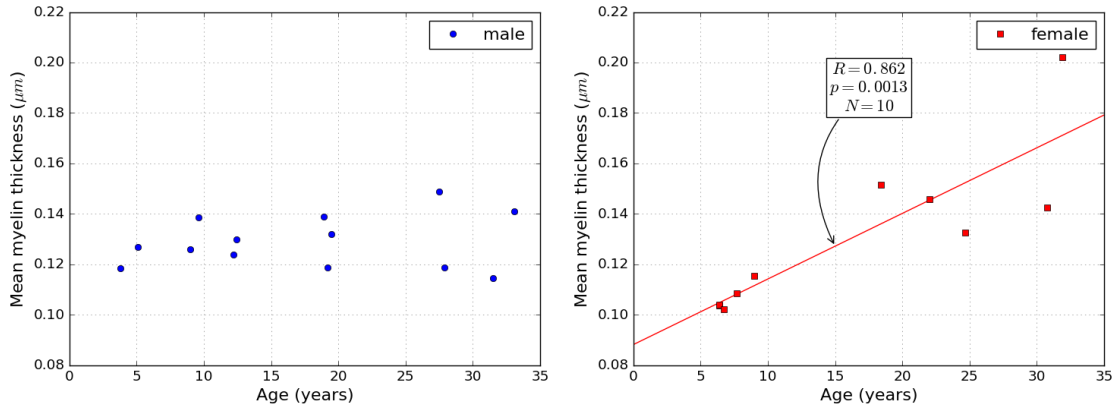


Figure 4.19: Average of the mean myelin thickness values of the myelinated axons in function of age, for only the male subjects (left) or only the female subjects (right). The linear regression for the male (female) subjects is shown in a solid blue (red) line, with corresponding Pearson correlation coefficients and p-values. The Pearson correlation coefficient for the male subjects is $R = 0.18$ with $p = 0.56$, while for the female group we get $R = 0.86$ with $p = 1.3 \times 10^{-3}$.

Focusing on each age group in particular, we notice a difference in the mean myelin thickness value between the male subjects and female subjects for both age groups. Comparing the the male and female subjects for each of the age groups, shown in Fig. 4.20, we observe that the young female subjects have lower mean myelin thickness than their young male counterparts ($p = 8.1 \times 10^{-3}$). This is interesting since the geometric means of the axon areas of young females are typically larger than the axon areas of the young male subjects, previously shown in Fig. 4.14. This means that despite having slightly larger cross-section areas, the myelinated axons of young female subjects are surrounded by a thinner myelin sheath than the myelinated axon of the young male subjects.

We also observe a small difference in the mean myelin thickness values between

old female subjects and old male subjects. Performing a one-sided Mann–Whitney U test, the old female subjects have a larger mean myelin thickness value than their male counterparts ($p = 0.026$). As opposed to the young females, the old female subjects present a slightly thicker myelin sheath than the old male subjects, which is expected since old female subjects have slightly larger axon areas.

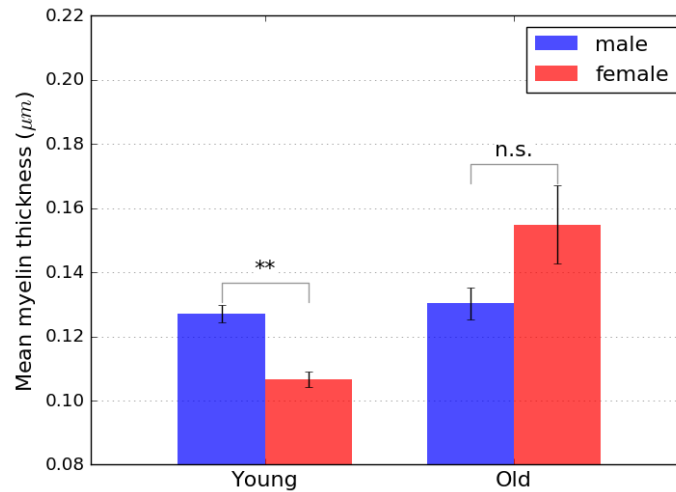


Figure 4.20: Average of the mean myelin thickness values of the myelinated axons for the 2 age groups, stratified by sex. For each age group, a two-sided Mann–Whitney U test was performed on the myelin thickness values of all male and female subjects in that age group. In this figure, n.s. stands for not significant. There is a statistical significant difference in the mean myelin thickness values between the young males and young females ($p = 8.1 \times 10^{-3}$). The difference between the old male subjects and the old female subjects is considered not significant ($p = 0.051$).

There is an observed correlation between the mean myelin thickness and the CII values for all subjects, as shown in Fig. 4.21. Although this correlation is considered significant ($p = 0.015$), it is not as significant as the correlation with the subjects' age. This would imply that the CII measurement is not heavily influenced by the mean myelin thickness.

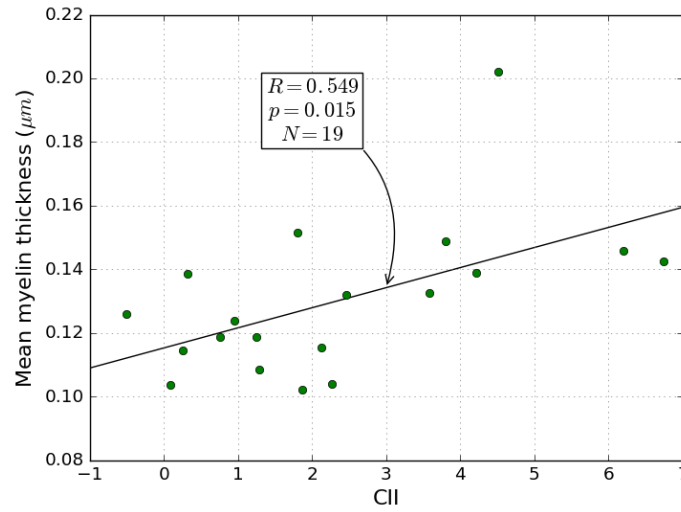


Figure 4.21: Average of the mean myelin thickness values of the myelinated axons in function of CII for all subjects. The linear regression for all subjects is shown in a solid line. The Pearson correlation coefficient for all subjects is $R = 0.55$ with $p = 0.015$ ($N = 19$). The Pearson correlation coefficient for the male subjects is $R = 0.68$ with $p = 0.046$ ($N = 9$), while for the female group we get $R = 0.59$ with $p = 0.076$ ($N = 10$).

4.3.2 Variance of myelin thickness

Another point related to the myelin thickness to examine is the variation of the myelin thickness along the axolemma and its possible dependence on age. In other words, we ask if the myelin sheath of older subjects has a less constant thickness along the axon contour, possibly due to remyelination.

In order to study this behavior, we calculated the standard deviation of the myelin thickness distribution for each axon, and determined its average for all axons in each subject. The subjects analyzed have an average of $0.0131 \mu m$ for the myelin thickness standard deviation.

According to Fig. 4.22, we observe that the axonal deviation of the myelin thickness shows no dependence on the age of the subjects. When separating by sex, the variation of the myelin thickness still shows no correlation with age. This indicates that the myelin sheath has a characteristic thickness variation that does not change

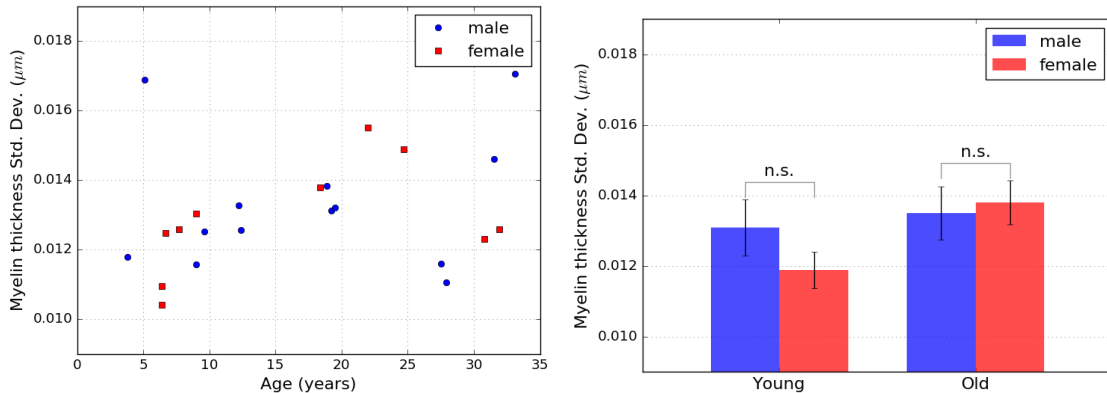


Figure 4.22: Variation of the myelin thickness per axon in function of the age the subjects, stratified by sex. The correlation of the variation of the myelin thickness with age for all subjects is $R = 0.29$, with $p = 0.18$. Separating by age group and sex, we observe that there is no significant difference between the male subjects and the female subjects, either for the young group, or for the old group.

with age. In other words, the remyelination process is not associated with an increase of the myelin thickness variance.

Note that there is also no significant correlation between the variation of myelin thickness and CII, as shown in Fig. 4.23.

4.3.3 G-ratio

The relationship between the axon and its surrounding myelin sheath is crucial to the physiological function of a myelinated axon. Both the conduction velocity of the electric signal propagated along the myelinated axon and the energy efficiency carrying that signal depend on the proportion of myelin to axon. This balance is measured by the myelinated axon g-ratio, i.e., the ratio of the inner axon diameter (d) to the outer fiber diameter (D). This parameter, a highly reliable ratio for assessing axonal myelination, is considered to be optimized in order to obtain the maximum efficiency in conduction while optimizing physiology [1].

Rushton was the first to derive the theoretical estimate of 0.6 for the optimal g-ratio [21]. In the case of a generic myelinated axon with a constant g-ratio $g =$

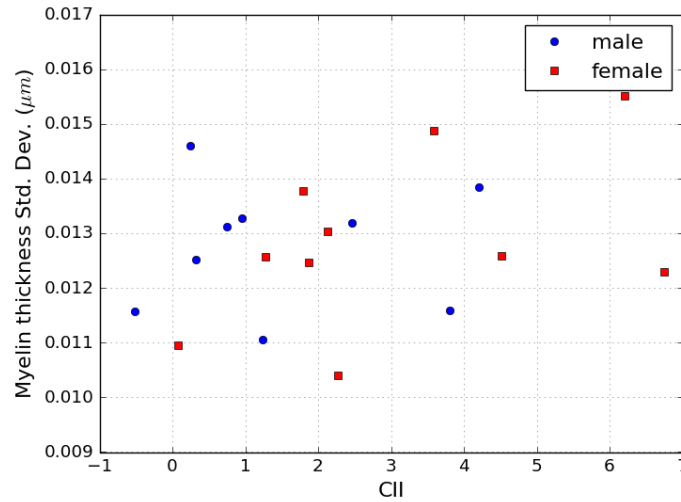


Figure 4.23: Variation of the myelin thickness per axon in function of CII, stratified by sex. There is no significant correlation between these values and the cognitive profile ($p = 0.18$). This remains true when considering only the male subjects ($p = 0.88$) or only the female subjects ($p = 0.18$).

d/D , the conduction velocity v is proportional to the fiber diameter D according to $v \propto Dg\sqrt{-\log g}$. Therefore, the maximum conduction velocity is achieved for $g \approx 0.6$ [21]. Posterior studies based on fundamental biophysical properties describing axonal structure and function show that for the central nervous system, the optimal g-ratio is 0.77 [1].

In order to calculate the g-ratio, we estimate the diameters of the inner axon and the outer fiber as the diameter of an equivalent circle with equal area, as shown in Fig. 4.24. Therefore, for each axon, we calculate the g-ratio via the ratio of the area of the inner myelinated axon to the area of the nerve fiber, according to

$$g = \frac{\text{axon diameter}}{\text{fiber diameter}} = \sqrt{\frac{\text{axon area}}{\text{fiber area}}} . \quad (4.8)$$

Note that we would get the same result if we mapped both cross-sections to their equivalent ellipses and calculated the ratio of their corresponding axes. We use the areas of the inner axon and the fiber area to estimate the corresponding diameters,

since these measurements are unaffected by small changes in the contour of the axons.

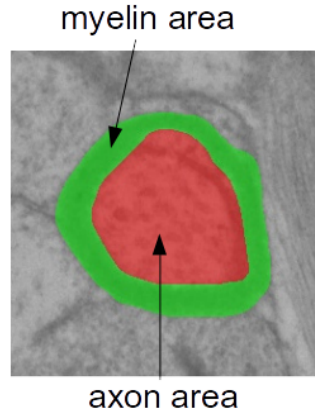


Figure 4.24: Diagram of the cross-section of a myelinated axon, showing the inner axon area (in red) and the outer myelin area (in green). The total fiber area is given by the axon area plus the myelin area. The g-ratio is given by the ratio of the axon diameter to the fiber diameter, as explained in Eq. (4.8).

Using the formula from Eq. (4.8), we calculate the g-ratio values for each axon and, subsequently, determine the average g-ratio for each subject. Across all subjects, the average g-ratio value is 0.762, very close to the predicted value in Ref. [1]. Taking the age of the subjects into account, we observe that the average g-ratio of the myelinated axons decreases with age ($p = 0.049$), as shown in Fig. 4.25.

However, when the analysis is stratified by sex, we find that while the average g-ratio of male subjects does not change with age, remaining close to the predicted value of 0.77 [1]. On the other hand, the g-ratio of female subjects has a significant decline with age ($p = 1.9 \times 10^{-3}$), starting at values higher than the predicted g-ratio value for the younger subjects, and reaching lower g-ratio values for the older subjects. This sex dichotomy is intimately related to the behavior observed for the mean myelin thickness for the male and female subjects separated, shown in Fig. 4.19. In fact, since the axon areas were shown not to correlate with age, the g-ratio dependence on the age of the female subjects is entirely due to the correlation of the mean myelin thickness with age. Therefore, the observed decrease in g-ratio values with increasing age for

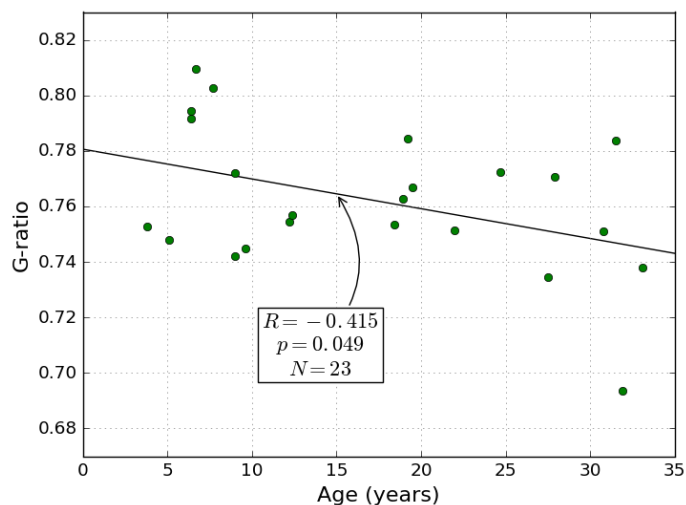


Figure 4.25: G-ratio values of the myelinated axons in function of the age of the 23 subjects analyzed. The linear regression is drawn in a solid line, with corresponding Pearson correlation coefficient and p-value.

female subjects is due to the increased myelin thickness for these same subjects. An extreme example comes from the old female subject AM041, which has a low value of g-ratio of 0.694, which comes entirely from having a very high mean myelin thickness of $0.202 \mu m$, compared to the total average mean myelin thickness of $0.130 \mu m$.

This decrease in g-ratio with age, associated to an increase of the myelin thickness, could be evidence of a higher rate of remyelination in the female subjects, compared to their male counterparts. Considering the fact that the female subjects display a larger loss of myelinated axons from young to old, another possibility to explain the observed g-ratio behavior for female subjects is that myelinated axons with a high g-ratio and corresponding thinner myelin sheaths might die more frequently in female subjects. That is to say, the increased loss of myelinated axons observed for female subjects could be concentrated on the myelinated axons with lower values of myelin thickness.

Looking at each age group individually, we once again notice the statistically significant difference in the g-ratio values between young male subjects and young female subjects ($p = 8.2 \times 10^{-3}$). On the other hand, the g-ratio values for the old

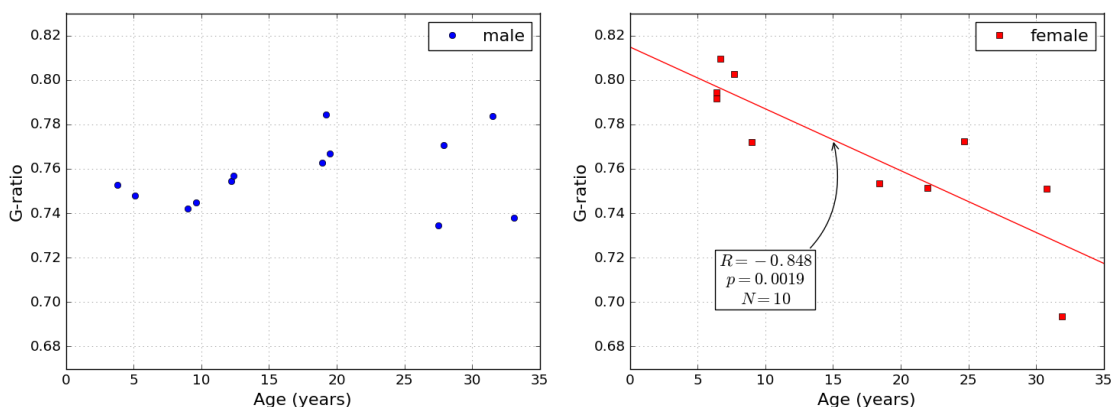


Figure 4.26: G-ratio values of the myelinated axons in function of age, for only the male subjects (left) or only the female subjects (right). The linear regression for female subjects is shown in a solid red line, with corresponding Pearson correlation coefficient and p-value. For the male subjects, the Pearson correlation coefficient is $R = 0.25$, with $p = 0.42$.

male subjects are similar to the ones for their female counterparts, as expected as any difference in the myelin thickness between old male and old female subjects is associated with a similar difference in the axon areas.

This sex dichotomy is also present in the standard deviation of the g-ratio, as shown in Fig. 4.28. This is interesting since this increase in variation of the g-ratio values for female subjects is observed despite the absence of any increase of variation in either the myelin thickness or the axon areas.

Considering the influence of g-ratio on the CII of the subjects, we analyzed their correlation, shown in Fig. 4.29. Accordingly, we detect no significant correlation between the g-ratio values and the CII of the subjects analyzed, even when separating the subjects by sex.

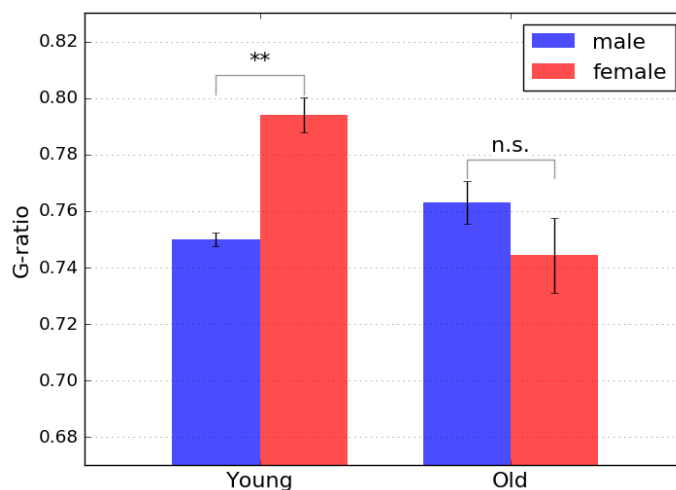


Figure 4.27: G-ratio values of the myelinated axons for the 2 age groups, stratified by sex. For each age group, a two-sided Mann–Whitney U test was performed on the g-ratio values of all male and female subjects in that age group. In this figure, n.s. stands for not significant. There is a statistical significant difference in the g-ratio values between the young males and young females ($p = 8.1 \times 10^{-3}$).

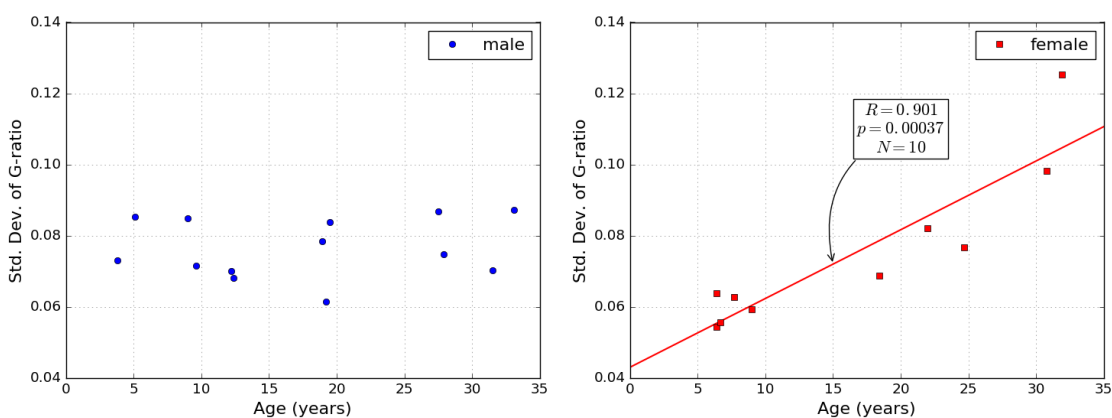


Figure 4.28: Variation of the g-ratio values of the myelinated axons, measured by its standard deviation, in function of age, for only the male subjects (left) or only the female subjects (right). The linear regression for female subjects is shown in a solid red line, with corresponding Pearson correlation coefficient and p-value. For the male subjects, the Pearson correlation coefficient is $R = 0.15$, with $p = 0.64$.

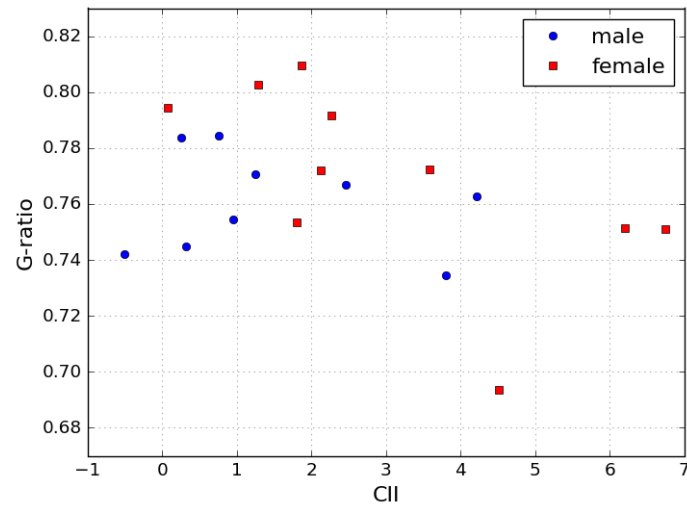


Figure 4.29: G-ratio values of the myelinated axons in function of CII for all subjects, separated by sex. The Pearson correlation coefficient for all subjects is $R = -0.39$ with $p = 0.10$ ($N = 19$).

Chapter 5

Conclusions

In this dissertation, we present a novel recognition algorithm capable of recognizing not only the myelinated axons but also their surrounding myelin sheath. This is a fully automatic algorithm, with an average precision of 95% and a sensitivity of 90%. It is also able to fully capture the shape of the myelinated axons, having an average overlap ratio value of 0.92, comparable to the same ratio between the markings of two persons. Furthermore, the recognition rates do not correlate with age, thus the algorithm performs independently of the age of the subjects analyzed.

We present a systematic procedure to quantify differences between samples of nerve fibers taken from distinct groups. This method allows us to objectively identify the most appropriate set of features that best discriminates samples from distinct groups such as young and old, but is also applicable to other conditions (development, disease) as well as for comparisons across regions of interest in the same species and across different species. By using a feature selection algorithm, this method has the advantage of considering simultaneously an extensive list of features, without the risk of ignoring features that could have been overlooked. Furthermore, this measurements are performed automatically using an algorithm, instead of relying on conventional stereological techniques. The analysis in this method is done in an incremental manner, as we perform an exhaustive comparison of single, pairs and trios of features. We

also perform a search for the set of features resulting in the highest accuracy, looking for the set that provides the most accurate group separation, regardless of the number of features in that set. In this analysis, we provide a comprehensive list of features that may unveil particularly interesting characteristics in three main aspects of nerve fibers: macroscopic features (characteristics of collections of axons), morphologic features (characteristics of individual axons) and structural features (characteristics of the relationship between different axons in each sample).

In the case of the specific application to the problem of aging we find that, when considering single features individually, density related features provide the best age separation. These include fraction of occupied area, effective local density, axon density, number of axons as well as third/second/first nearest neighbor mean distance. This is expected, since it is known that one of the most pronounced effects of aging in the fornix is the loss of myelinated axons [5].

We find that the fraction of occupied area provides the best single feature accuracy. This may be an indication that the actual axon area through which information is transmitted might be more relevant to aging than the number of elements that can transmit it, i.e., the number of axons. The mean hexagonality index also provides a good separation between the samples, with the young group having a higher mean hexagonality index, which shows that the young group has a more regular or ordered angular structure, i.e., the axons surrounding each axon are distributed more evenly. This regularity is partially lost during aging, possibly due to temporally spaced loss of axons from different regions, with temporally spaced gliosis filling in.

Features related to the area and shape of the contour of the myelinated axon, i.e., morphologic features, are not statistically different for the two age groups, as reflected by the low accuracies attained when discriminating between age groups using those features individually. This indicates that myelinated axons are lost irrespectively of their area or shape.

In the analysis with two features, an exhaustive search reveals that many pairs of

features can provide accuracies near 90%. The most relevant pair is formed by the combination of fraction of occupied area and effective local density. This pair provides the highest accuracy in the age group separation as well as a large scatter distance between the two classes. This pair is particularly interesting, since by replacing density with effective local density, one corrects the classification of a few samples that would have been assigned to the wrong class if using the pair formed by the density with the fraction of occupied area. We find that the effective local density is, at least in the study of aging, more sensitive to axon loss than simple density. This may be the case because it is sensitive to structural changes in the spatial relationships among axons, specifically the non-random presence of axon-free regions. In turn, this may reflect the fact that axons with similar properties (size, origin, etc.) may be spatially clustered. If so, then the loss of axons in these clusters might reflect their selective vulnerability.

When considering sets of three features, the highest accuracy attained is 91%, resulting in an improvement of the classification accuracy of only 1%. That is, the inclusion of another feature only corrects, at best, the classification of one sample. We also look for the set of features (regardless of their number) that can provide the highest possible accuracy using a heuristic search, and find that the discrimination can be improved to as much as 94%, but needing a set of 6 particular features. Therefore, two features are enough to characterize the separation between the two age groups. Note that this conclusion is valid for our case study, since other cases might need more (or less) features to confidently discriminate between the two different classes.

Regarding the behavior of the measured axon properties with age, we confirmed the results of previous studies [5, 10] and showed that the myelinated axon density as well as the fraction of occupied area decrease with age. However, we do observe a difference between old male subjects and old female subjects. As female subjects get older, they lose a higher percentage of the myelinated axons in the fornix of the brain than their male counterparts. Associated with a lack of change in the fornix

area, it implies that there is also a greater loss in numbers of myelinated axons with age for female subjects. The sex difference in the fraction of occupied axon areas and in the myelinated axon density reveal a systematic axon area difference between male and female subjects, with female subjects having larger typical axon areas than male subjects. On the other hand, we observe similar values of fraction of occupied fiber area for male and female subjects. This would imply that young male subjects have similar structural packing properties to the young female subjects, while old female subjects typically have larger axons in lower numbers, compared to the old male subjects.

The axon area distribution of each axon follows a log-normal distribution, which is characteristic of a stochastic geometric growth model, where each growth step of the axon would be proportional to its size. Regarding the age influence, we show that the average axon area shows no dependence on the age of the subjects. This indicates that the loss of axons with age happens independently of their size, i.e., myelinated axons with different cross-section areas die at equal rates with age.

Considering the myelin sheath properties, we observe that there is a slight increase of the myelin thickness with age. However, this overall behavior is only due to the increase observed for female subjects, while the myelin thickness remains unaltered with age for male subjects. The myelinated axons of young female subjects are surrounded by a thinner myelin sheath than the myelinated axons of the young male subjects, despite having slightly larger cross-section areas. On the other hand, the old female subjects present a slightly thicker myelin sheath than the old male subjects, which is expected since old female subjects have slightly larger axon areas. We also observe that the characteristic thickness variation in each myelinated axon does not change with age. In other words, the remyelination process associated with myelin repair is not associated with an increase of the myelin thickness variance.

This behavior of the myelin thickness, influences the behavior of the g-ratio of the myelinated axons, as it decreases slightly with age. In a similar fashion, the g-ratio of

female subjects has a significant decrease with age, while the average g-ratio of male subjects does not change with age. This decrease with age in female subjects is due to the increase of myelin thickness with age for these same subjects. The decrease in g-ratio with age, associated to an increase of the myelin thickness, could be evidence of a higher rate of remyelination in the female subjects. Another possibility is the fact that myelinated axons with a high g-ratio and corresponding thinner myelin sheaths might die more frequently in female subjects. We also observe an increase in variation of the g-ratio values for female subjects despite the absence of any increase of variation in either the myelin thickness or the axon areas.

In summary, feature selection is a novel and useful methodology to choose the best set of features to describe the samples and detect differences between classes of myelinated axons. In this specific case study of aging, we conclude that only two features are enough to discriminate the samples into their proper age groups, namely the combination of fraction of occupied area and effective local density.

It is also important to note that the general methodology for feature detection presented here should be adaptable to enable the observation of changes in microscopic features caused by brain pathologies in neurodegenerative diseases like Alzheimer's Disease or by developmental disorders as well as pathological or developmental changes in other organ systems like the kidney or the pancreas. Moreover, our methodology can be potentially extended to feature detection techniques at more macroscopic scales such as MRI.

Appendix A

Calculation of the Orientation Angle and Flattening of each Contour

The orientation angle, eccentricity and flattening of a polygon are calculated from its 2^{nd} order image moments [15, 16, 18].

A.1 Image Moments

The moments of a 2D object defined by a function $f(x, y)$ are given by

$$M_{pq} = \iint x^p y^q f(x, y) \, dx \, dy . \quad (\text{A.1})$$

In the case of an object in a binary image, $f(x, y) = 1$ inside the object and $f(x, y) = 0$ outside. Notice that the area of the object is given simply by the 0^{th} order moment M_{00} . Instead of the ordinary moments, we usually use the central moments defined below, as they don't depend on the object location

$$\mu_{pq} = \iint (x - \bar{x})^p (y - \bar{y})^q f(x, y) \, dx \, dy , \quad (\text{A.2})$$

where $\bar{x} = M_{10}/M_{00}$ and $\bar{y} = M_{01}/M_{00}$ are the centroid positions of the object, i.e., the center of mass of the object. We use the normalized central moments defined as

$$\mu'_{pq} = \frac{\mu_{pq}}{\mu_{00}}, \quad (\text{A.3})$$

where the central moments are normalized by the object area $\mu_{00} = M_{00}$.

The object orientation can be determined by first setting up the covariance matrix with the 2^{nd} order central moments

$$\text{Cov}[I(x, y)] = \begin{bmatrix} \mu'_{20} & \mu'_{11} \\ \mu'_{11} & \mu'_{02} \end{bmatrix}, \quad (\text{A.4})$$

and calculating their eigenvalues and eigenvectors. The eigenvectors correspond to the major and minor axis of the object and its orientation is the angle of the eigenvector associated with the largest eigenvalue, corresponding to the major axis. The orientation angle is given by

$$\Theta = \frac{1}{2} \arctan \left(\frac{2\mu'_{11}}{\mu'_{20} - \mu'_{02}} \right), \quad (\text{A.5})$$

and the eigenvalues are

$$\lambda_i = \frac{\mu'_{20} + \mu'_{02}}{2} \pm \frac{\sqrt{4\mu'_{11}{}^2 + (\mu'_{20} - \mu'_{02})^2}}{2}. \quad (\text{A.6})$$

By considering only the moments up to the 2^{nd} order, the original object is equivalent to an ellipse with an eccentricity given by

$$e = \sqrt{1 - \left(\frac{b}{a}\right)^2} = \sqrt{1 - \frac{\lambda_-}{\lambda_+}}, \quad (\text{A.7})$$

where a is the semi-major axis, b is the semi-minor axis. λ_+ and λ_- are the largest and smallest eigenvalues, respectively. As a simpler alternative to the eccentricity,

and more appropriate to our objects, the compression of the object along its major axis can also be described by the flattening f , given by

$$f = 1 - \frac{b}{a} = 1 - \sqrt{\frac{\lambda_-}{\lambda_+}} . \quad (\text{A.8})$$

A.2 Calculate Image Moments

For a polygon described by its contour points, the image moments can be calculated by using the Green's theorem:

$$\oint_C (L dx + M dy) = \iint_D \left(\frac{\partial M}{\partial x} - \frac{\partial L}{\partial y} \right) dx dy . \quad (\text{A.9})$$

By choosing the functions $M(x, y)$ and $L(x, y)$, one can convert an area integral of a function (e.g., moment) into a contour integral. For a set of discrete points determining a contour, the integral is equivalent to a sum.

For example, the area of the polygon D with contour C can be calculated by choosing $M(x, y)$ and $L(x, y)$ such that $\frac{\partial M}{\partial x} - \frac{\partial L}{\partial y} = 1$. As such, the area is given by the following contour integral

$$\begin{aligned} A &= \oint_C x dy \\ &= - \oint_C y dx \\ &= \frac{1}{2} \oint_C (-y dx + x dy) , \end{aligned} \quad (\text{A.10})$$

which can be converted into the following sum for a set of discrete contour points

$$\begin{aligned}
A &= \frac{1}{2} \left| \sum_{i=1}^n x_i (y_{i+1} - y_{i-1}) \right| \\
&= \frac{1}{2} \left| \sum_{i=1}^n y_i (x_{i+1} - x_{i-1}) \right| \\
&= \frac{1}{2} \left| \sum_{i=1}^n x_i y_{i+1} - x_{i+1} y_i \right|. \tag{A.11}
\end{aligned}$$

This last equation is known as the shoelace formula for determining the area of a polygon, with the vertices ordered sequentially in the plane. Normally this sequence of points is given counterclockwise, so that the sum gives a positive value. The 1st and 2nd order moments of a polygon are given by the following formulas

$$M_{10} = \frac{1}{6} \sum_i d_i (x_i + x_{i+1}), \tag{A.12}$$

$$M_{01} = \frac{1}{6} \sum_i d_i (y_i + y_{i+1}), \tag{A.13}$$

$$M_{20} = \frac{1}{12} \sum_i d_i (x_i^2 + x_i x_{i+1} + x_{i+1}^2), \tag{A.14}$$

$$M_{02} = \frac{1}{12} \sum_i d_i (y_i^2 + y_i y_{i+1} + y_{i+1}^2), \tag{A.15}$$

$$M_{11} = \frac{1}{24} \sum_i d_i [x_i (2y_i + y_{i+1}) + x_{i+1} (y_i + 2y_{i+1})], \tag{A.16}$$

where $d_i = x_i y_{i+1} - x_{i+1} y_i$. From these moments, one can calculate the normalized central moments according to

$$\mu'_{20} = \frac{M_{20}}{M_{00}} - \bar{x}^2, \tag{A.17}$$

$$\mu'_{02} = \frac{M_{02}}{M_{00}} - \bar{y}^2, \tag{A.18}$$

$$\mu'_{11} = \frac{M_{11}}{M_{00}} - \bar{x} \bar{y}. \tag{A.19}$$

Appendix B

Circular Statistics

B.1 Angular Average

When dealing with periodic quantities, as is the case of angles, the calculation of the average and variance of a distribution is not trivial and the arithmetic formulas for the mean and standard deviation no longer apply [22, 23].

In the specific case of angles, they have a period of 2π , as an angle α is equivalent to any other angle $\alpha + 2k\pi$, with k being an integer number. For example, the angle $\pi/3$ radians = 60° is equivalent to $7\pi/3$ radians = 420° , $-5\pi/3$ radians = -300° and so on. As such, we only need to define angles in the region $]-\pi, \pi]$ (or any other interval of period 2π).

Due to this periodic characteristic, the arithmetic mean of a set of angles is not well defined and can no longer be used to calculate their average. For example, for the set of the 2 angle values 140° and 170° , their arithmetic mean is 155° . However, if one rotates the same set clockwise by 20° , therefore getting the angles 160° and -170° , the arithmetic mean is now -5° , instead of the expected average of 175° .

In order to calculate the average (and other statistics) of a set of angles, it is recommended to convert the set of angles into complex numbers of unit magnitude $z = e^{i\theta}$, where θ is the angle. These unit vectors in the complex plane incorporate the

period characteristic of angles, as different equivalent angles map to the same unit vector. One can calculate the mean resultant vector as

$$\bar{\rho} = \frac{1}{N} \sum_{n=1}^N z_n , \quad (\text{B.1})$$

and the average angle is given by the argument of the mean vector

$$\bar{\theta} = \arg \bar{\rho} . \quad (\text{B.2})$$

Considering that $z = \cos \theta + i \sin \theta$, the average angle can also be written simply as

$$\bar{\theta} = \arctan \left(\frac{\sum_{n=1}^N \sin \theta_n}{\sum_{n=1}^N \cos \theta_n} \right) . \quad (\text{B.3})$$

For the example set given above, this formula gives 175° for the average angle, as expected.

B.2 Circular Distributions

The equivalent of the normal distribution for angles is the wrapped normal distribution, which probability density function is given by

$$f_{WN}(\theta) = \frac{1}{\sigma\sqrt{2\pi}} \sum_{k=-\infty}^{\infty} \exp\left(-\frac{(\theta - \mu + 2\pi k)^2}{2\sigma^2}\right) , \quad (\text{B.4})$$

where μ and σ are the mean and standard deviation of the ‘unwrapped’ normal distribution.

This wrapped normal distribution, shown in Fig. B.1, can be understood as the ‘wrapping’ of the normal distribution around the circle of unit radius. As one wraps the distribution around the unit circle, the probability of a certain angle results from the sum of the probabilities of the ‘wrapped’ distribution at that particular angle.

The expected value of the circular variable $z = e^{i\theta}$ for this distribution is $\langle z \rangle =$

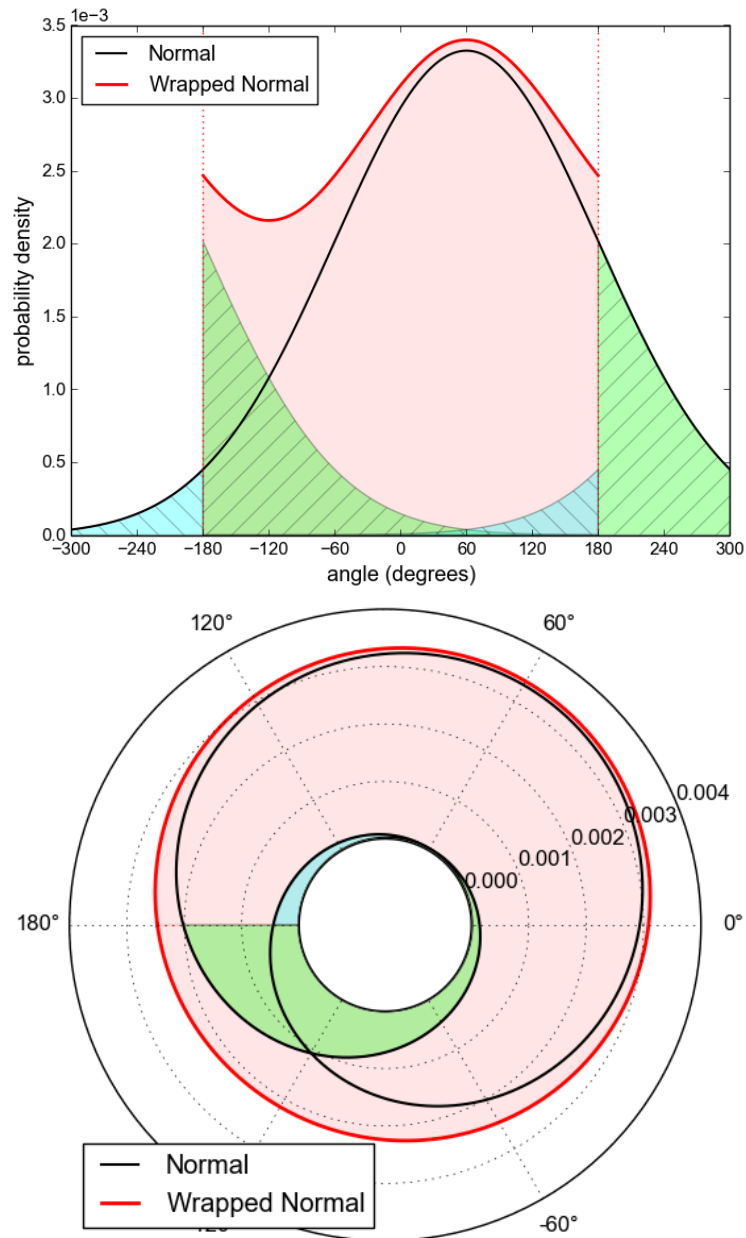


Figure B.1: Example of a wrapped normal distribution (red solid line) with $\mu = 60^\circ$ and $\sigma = 120^\circ$ in (a) cartesian representation and (b) polar representation. The wrapped normal distribution originates from the wrapping of the normal distribution (black solid line). The filled areas in green and cyan represent the wrapping of the tails of the normal distribution.

$e^{i\mu-\sigma^2/2}$. As such, the average angle is simply

$$\theta_\mu = \arg\langle z \rangle = \mu , \quad (\text{B.5})$$

while the circular standard deviation, measuring the dispersion of the wrapped normal distribution, is

$$s = \sqrt{-2 \log R} = \sigma , \quad (\text{B.6})$$

where $R = |\langle z \rangle| = e^{-\sigma^2/2}$ is the length of the mean resultant vector.

In the case of the circular uniform distribution, as is expected for a random set of angles, the probability density function is just

$$f_{UC}(\theta) = \frac{1}{2\pi} . \quad (\text{B.7})$$

For this particular case, the average angle is undefined since $\langle z \rangle = 0$. This is because there is no clear angle value around which all the other angles are dispersed, i.e., the dispersion around any particular angle is equal to all other angles. Similarly, the circular standard deviation is $\sigma = \infty$, corresponding to the dispersion of a ‘unwrapped’ distribution with no limits.

B.3 Orientation Angles

In the case of orientation angles ϕ , the period is now equal to π . As such, one needs to rewrite the circular variable as $z = e^{i2\phi}$, to reflect the new periodic conditions. After calculating the resultant mean vector $\bar{\rho} = \frac{1}{N} \sum_{n=1}^N z_n$, the average orientation is equal to

$$\bar{\phi} = \frac{1}{2} \arg \bar{\rho} = \frac{1}{2} \arctan \left(\frac{\sum_{n=1}^N \sin(2\phi_n)}{\sum_{n=1}^N \cos(2\phi_n)} \right) . \quad (\text{B.8})$$

Similarly, the orientational standard deviation is equal to

$$s = \sqrt{-\frac{1}{2} \log |\bar{\rho}|} . \quad (\text{B.9})$$

This is equivalent to converting the orientation angles to circular angles by multiplying by a factor of 2 and using the circular statistics formulas to calculate the average angle and circular standard deviation. The orientation average and orientational standard deviation are given by dividing the corresponding circular average and circular standard deviation by a factor of 2.

B.4 Orientational Order Parameter

Another way to measure the order (or dispersion) of orientation angles is the orientational order parameter, commonly used in calculating the orientational order of bonds or describing the order of nematic liquid crystals. The orientational order parameter S is defined as the average of the second Legendre polynomial

$$S = \langle P_2(\cos(\phi - m)) \rangle = \left\langle \frac{3 \cos^2(\phi - m) - 1}{2} \right\rangle , \quad (\text{B.10})$$

where m is the preferred direction. The orientational order parameter can take values in the range $[0, 1]$, where $S = 1$ represents a set of perfectly aligned orientations. Considering this definition of order, the mean direction m can be defined as the value that maximizes S . By rewriting the order parameter S as

$$S = \frac{3 [\langle \cos(2\phi) \rangle \cos(2m) + \langle \sin(2\phi) \rangle \sin(2m)] + 1}{4} , \quad (\text{B.11})$$

its maximum, as given by the equation $\frac{\partial S}{\partial m} = 0$, results in

$$\tan(2m) = \frac{\langle \sin(2\phi) \rangle}{\langle \cos(2\phi) \rangle} , \quad (\text{B.12})$$

which gives the same average direction as defined previously in Eq. (B.8). When replacing m by the average orientation, the order parameter S is related to the orientational standard deviation σ according to the following equation

$$S = \frac{1 + 3 e^{-2\sigma^2}}{4}, \quad (\text{B.13})$$

where we use the following equivalence

$$\begin{aligned} \langle z \rangle &= \langle e^{i2\phi} \rangle = \langle \cos(2\phi) \rangle + i \langle \sin(2\phi) \rangle \\ &= e^{-2\sigma^2} e^{i2m} = e^{-2\sigma^2} [\cos(2m) + i \sin(2m)]. \end{aligned} \quad (\text{B.14})$$

This equivalence between the orientational standard deviation and the orientational order parameter in describing the dispersion of the orientation angles is illustrated in Fig. B.2.

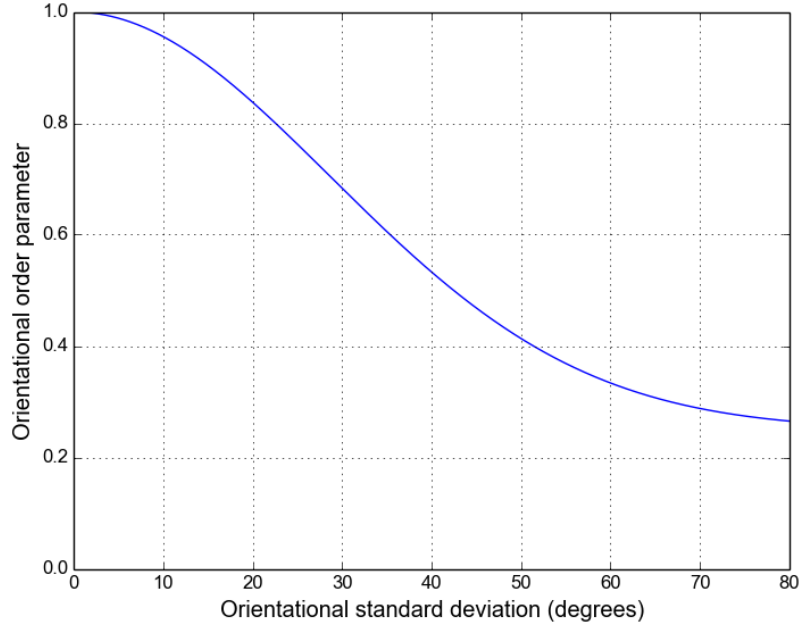


Figure B.2: Relationship between the orientational order parameter and the orientational standard deviation.

Although the orientational order parameter can vary from 0 to 1, in the case of a

random set of orientation angles, described by the orientational uniform distribution $f(\phi) = \frac{1}{\pi}$, the orientation order parameter is, on average, $S = 0.25$.

Appendix C

Outliers

C.1 Probability Plot

By looking at the probability plot of the mean orientational order parameter for each image, we notice that the order parameters for individual images tend to follow a normal distribution (especially in the upper values tail, for which we are evaluating if there are any outliers). Therefore, we expect that the mean order parameter for the subjects (calculated by collecting all axons in all images of a particular subject) would also follow a normal distribution, unless there was a consistent bias in the cut angle, when preparing the samples.

Considering the mean order parameter for each subject, the probability plot still shows some normality of the data (described by a linear fit), except in the upper tail. In fact, there are 2 (or possibly 4) subjects that deviate significantly from the linear fit (AM019 & AM144), which we suspect being outliers, due to a bias in the cut angle.

C.2 Box Plot

A method to confirm if these 2 subjects are indeed outliers involves plotting the order parameter distribution in a Tukey box plot. In this plot, any point outside

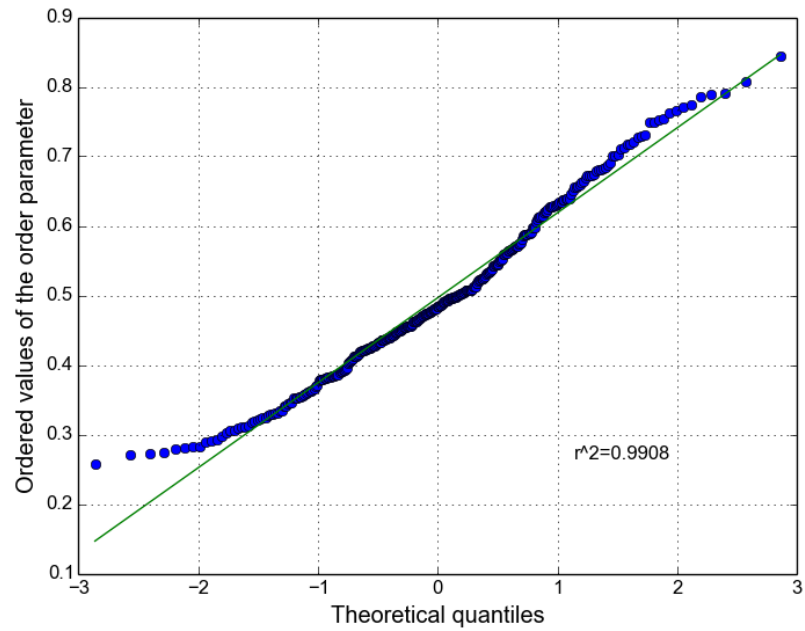


Figure C.1: Probability plot of the mean orientational order parameter for each image (N=328).

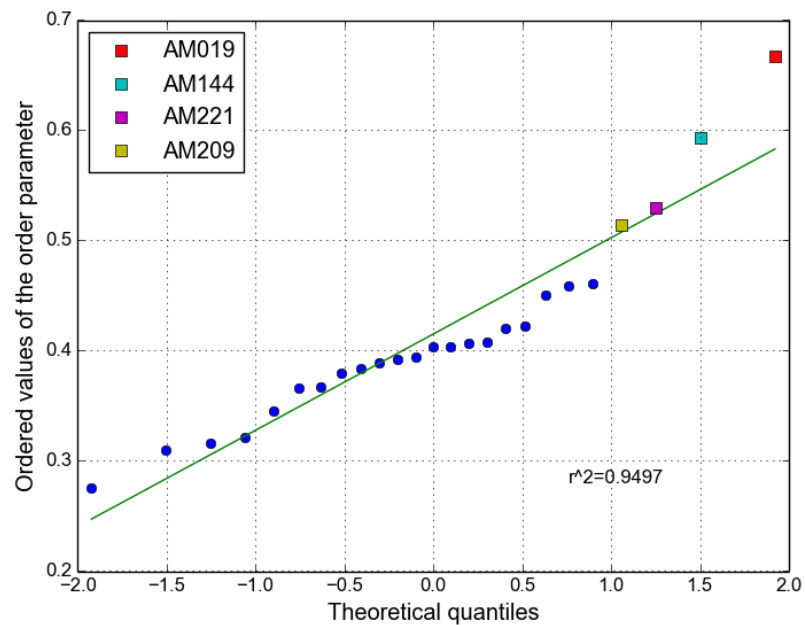


Figure C.2: Probability plot of the mean orientational order parameter for each subject (N=25).

the region $[Q_1 - 1.5 \times \text{IQR}, Q_3 + 1.5 \times \text{IQR}]$ is classified as an outlier. Q_1 and Q_3 are the 1st quartile and 3rd quartile, respectively (representing the 25% percentile and 75% percentile), while the IQR is the interquartile range, defined as $\text{IQR} = Q_3 - Q_1$. In a normal distribution, this criterion will classify 0.70% of all points as outliers. Assuming a normal distribution of the order parameter for all the 25 subjects, we expect a fraction (0.17) of the subjects outside the region defined by the whiskers $Q_1 - 1.5 \times \text{IQR}$ & $Q_3 + 1.5 \times \text{IQR}$. Instead, we find 2 subjects outside the region and classified as outliers: AM019 & AM144 (these 2 subjects have mean order parameters of 0.667 and 0.593 respectively, compared to the upper limit $Q_3 + 1.5 \times \text{IQR}$ of 0.576). Note that the probability of finding 2 or more subjects outside the region is 1.3%, assuming a normal distribution.

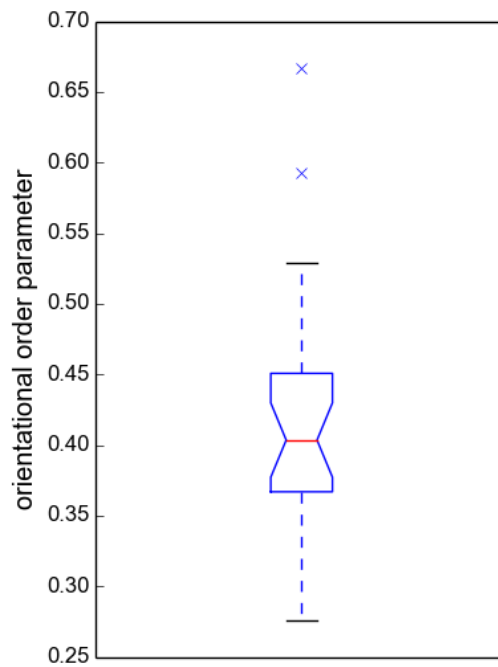


Figure C.3: Box plot of the mean orientational order parameter for each subject ($N=25$). There are 2 outliers in the upper tail of the distribution corresponding to subjects AM019 and AM144.

C.3 Permutation Test

A more robust (and non-parametric) method to detect outliers is by using the permutation test. In this resampling method, the subject labels for each individual image are randomly shuffled, therefore recreating a set of random subjects, each with the same initial number of images, selected from the total pool of 328 images. These recreated 25 random subjects have random order parameters that can be compared with the measured order parameters. If a subject has a mean order parameter that can't be replicated by this random shuffling process, it would be classified as an outlier. From the next 2 figures, we see that the subject AM019 is clearly an outlier, with no random value (out of the 10000 random runs) even approaching its measured order parameter. The next possible outlier (AM144) also looks to be an outlier. Focusing only on the orientational order parameter, we see that these 2 subjects (AM019 and AM144) are significantly distinct from the rest with $p < 10^{-4}$.

C.4 Summary

In summary, AM019 is clearly an outlier, while AM144 has a strong possibility of being one as well.

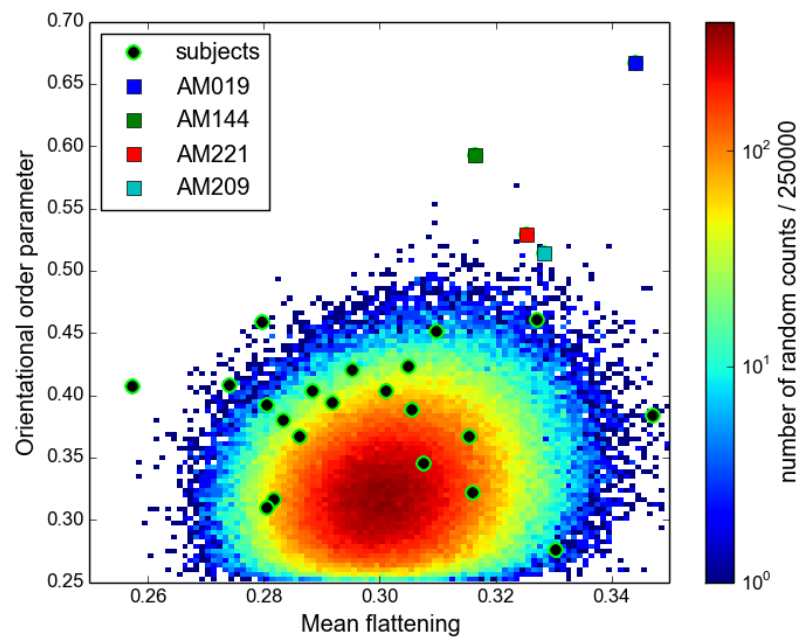


Figure C.4: Orientational order parameter in function of the mean flattening for the 25 subjects, compared with the random values obtained with the permutation test (10000 random runs, resulting in 250000 randomly recreated subjects).

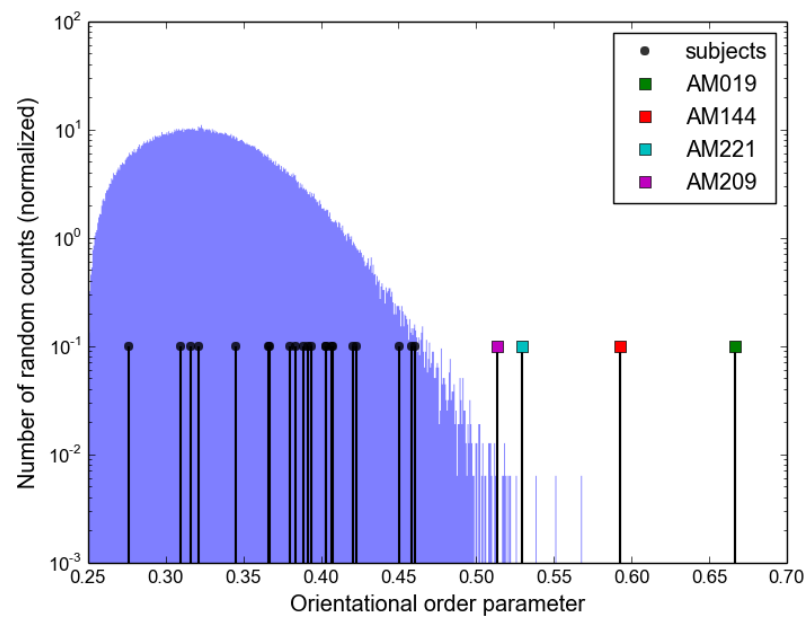


Figure C.5: Orientational order parameter of the 25 subjects, compared with the random values obtained with the permutation test (10000 random runs, resulting in 250000 randomly recreated subjects).

Appendix D

Nearest Neighbor Mean Distance for a Poisson Point Process

We consider a homogeneous (i.e., with spatially uniform statistical properties) Poisson point process [90] (i.e., with a random particle distribution) in \mathbb{R}^d , characterized by the uniform mean density $\rho > 0$.

Choosing the origin of the axes at a given particle of the system, $\omega_n(r)$ is defined as the probability density function (PDF) of the distance of its n -th nearest neighbor, i.e., the probability that for a particle at the origin, its n -th nearest neighbor is at a distance between r and $r + dr$, as shown in the equation

$$\omega_n(r) dr = \text{Prob}(r \leq |\mathbf{r}_n| < r + dr) , \quad (\text{D.1})$$

where \mathbf{r}_n is the spatial position of the n -th nearest neighbor of the particle located at the origin of the axes. To find $\omega_n(r)$ we generalize the calculation usually adopted for the case $n = 1$. For a Poisson point process, the positions of different particles are independent and the probability of having exactly N particles in an arbitrary volume V is

$$p(N, V) = \frac{(\rho V)^N}{N!} e^{-\rho V} . \quad (\text{D.2})$$

In this system, both the average number of particles in the volume V and its variance are given by

$$\langle N \rangle = \langle N^2 \rangle - \langle N \rangle^2 = \rho V . \quad (\text{D.3})$$

Considering the mutual independence of the positions of the particles, and using Eq. (D.2), we can write

$$\begin{aligned} \omega_n(r) dr &= p(n-1, V(r)) \cdot p(1, S(r) dr) \\ &= \frac{(\rho V(r))^{n-1}}{(n-1)!} e^{-\rho V(r)} \rho S(r) dr e^{-\rho S(r) dr} . \end{aligned} \quad (\text{D.4})$$

where $V(r)$ is the volume of the d -dimensional sphere of radius r and $S(r)$ is its external surface area so that $S(r) dr$ is the volume of the spherical shell between the radii r and $r + dr$. Note that because we are interested in the infinitesimal limit for dr the last exponential in Eq. (D.4) can be substituted simply by 1. In d dimensions

$$V(r) = \frac{\Omega_d}{d} r^d \quad (\text{D.5})$$

$$S(r) = \Omega_d r^{d-1} , \quad (\text{D.6})$$

where Ω_d is the complete solid angle in d dimensions (1 in $d = 1$, 2π in $d = 2$, 4π in $d = 3$, etc.). Thus we can finally write

$$\omega_n(r) = \rho \Omega_d r^{d-1} \frac{(\rho \frac{\Omega_d}{d} r^d)^{n-1}}{(n-1)!} e^{-\rho \frac{\Omega_d}{d} r^d} . \quad (\text{D.7})$$

Note that $\omega_n(r)$ is a well-normalized PDF, i.e., its integral between 0 and ∞ is equal to 1.

Mean Distance

The n -th nearest neighbor mean distance is given by

$$\langle r_n \rangle = \int_0^{\infty} r \omega_n(r) dr . \quad (\text{D.8})$$

By performing the change of variable

$$u = \rho \frac{\Omega_d}{d} r^d , \quad (\text{D.9})$$

we can write

$$\langle r_n \rangle = \frac{1}{(n-1)!} \left(\frac{d}{\rho \Omega_d} \right)^{1/d} \int_0^{\infty} du u^{n-1+1/d} e^{-u} . \quad (\text{D.10})$$

By using the definition of the Euler Gamma function [92] we obtain the final formula

$$\langle r_n \rangle = \left(\frac{d}{\rho \Omega_d} \right)^{1/d} \frac{\Gamma(n + 1/d)}{\Gamma(n)} . \quad (\text{D.11})$$

Note that for integer n , $\Gamma(n) = (n-1)!$

To obtain the scaling relation between $\langle r_n \rangle$ and rank n for large n we can use the following expansion for large z of the ratio of two Gamma functions [92],

$$\frac{\Gamma(z + \alpha)}{\Gamma(z + \beta)} = z^{\alpha - \beta} \left(1 + \frac{(\alpha - \beta)(\alpha + \beta - 1)}{2z} + \mathcal{O}(z^{-2}) \right) . \quad (\text{D.12})$$

In our case this gives

$$\frac{\Gamma(n + 1/d)}{\Gamma(n)} = n^{1/d} \left(1 - \frac{d-1}{2d^2 n} + \mathcal{O}(n^{-2}) \right) . \quad (\text{D.13})$$

Inserting this relation into Eq. (D.11), we obtain the general formula for the n -th nearest neighbor mean distance in d dimensions

$$\langle r_n \rangle = \left(\frac{d n}{\rho \Omega_d} \right)^{1/d} \left(1 - \frac{d-1}{2d^2 n} + \mathcal{O}(n^{-2}) \right) . \quad (\text{D.14})$$

Mean Distance in 2D

Applying our discussion to the case $d = 2$, we have

$$\langle r_n \rangle = \left(\frac{1}{\pi\rho} \right)^{1/2} \frac{\Gamma(n + 1/2)}{\Gamma(n)}. \quad (\text{D.15})$$

Using the relationship of Eq. (D.13), we obtain

$$\langle r_n \rangle = \left(\frac{n}{\pi\rho} \right)^{1/2} \left(1 - \frac{1}{8n} + \mathcal{O}(n^{-2}) \right). \quad (\text{D.16})$$

Moments

The moments $\langle r_n^k \rangle$ of the n -th nearest neighbor distance are given by

$$\begin{aligned} \langle r_n^k \rangle &= \int_0^\infty r^k \omega_n(r) \, dr \\ &= \left(\frac{d}{\rho\Omega_d} \right)^{k/d} \frac{\Gamma(n + k/d)}{\Gamma(n)}, \end{aligned} \quad (\text{D.17})$$

which has the following behavior for large n

$$\langle r_n^k \rangle = \left(\frac{d n}{\rho\Omega_d} \right)^{k/d} \left(1 - \frac{k(d-k)}{2d^2 n} + \mathcal{O}(n^{-2}) \right). \quad (\text{D.18})$$

In the case of $k = d$, Eq. (D.17) simplifies to the linear relationship

$$\langle r_n^d \rangle = \frac{d n}{\rho\Omega_d}. \quad (\text{D.19})$$

Bibliography

- [1] Taylor Chomiak and Bin Hu. What is the optimal value of the g-ratio for myelinated fibers in the rat CNS? A theoretical approach. *PLoS ONE*, 4(11):e7754, nov 2009.
- [2] L. Cruz, D. L. Roe, B. Urbanc, A. Inglis, H. E. Stanley, and D. L. Rosene. Age-related reduction in microcolumnar structure correlates with cognitive decline in ventral but not dorsal area 46 of the rhesus monkey. *Neuroscience*, 158(4):1509–1520, 2009.
- [3] I Guyon and A Elisseeff. An introduction to variable and feature selection. *Journal of Machine Learning Research*, 3:1157–1182, 2003.
- [4] Yvan Saeys, Iñaki Inza, and Pedro Larrañaga. A review of feature selection techniques in bioinformatics. *Bioinformatics*, 23(19):2507–2517, 2007.
- [5] Alan Peters, Claire Sethares, and Mark B. Moss. How the primate fornix is affected by age. *Journal of Comparative Neurology*, 518(19):3962–3980, 2010.
- [6] John P. Aggleton, Shane M. O’Mara, Seralynne D. Vann, Nick F. Wright, Marian Tsanov, and Jonathan T. Erichsen. Hippocampal-anterior thalamic pathways for memory: Uncovering a network of direct and indirect actions. *European Journal of Neuroscience*, 31(12):2292–2307, 2010.

- [7] Dale Purves, George J Augustine, David Fitzpatrick, William C Hall, Anthony-Samuel LaMantia, James O McNamara, and S. Mark Williams. *Neuroscience*. Sinauer, Sunderland, 3rd edition, 2004.
- [8] Michael P. Bowley, Howard Cabral, Douglas L. Rosene, and Alan Peters. Age changes in myelinated nerve fibers of the cingulate bundle and corpus callosum in the rhesus monkey. *Journal of Comparative Neurology*, 518(15):3046–3064, mar 2010.
- [9] James G Herndon, Mark B Moss, Douglas L Rosene, and Ronald J Killiany. Patterns of cognitive decline in aged rhesus monkeys. *Behavioural Brain Research*, 87(1):25–34, 1997.
- [10] César H Comin, João R Santos, Dario Corradini, Will Morrison, Chester Curme, Douglas L Rosene, Andrea Gabrielli, Luciano da F Costa, and H Eugene Stanley. Statistical physics approach to quantifying differences in myelinated nerve fibers. *Scientific Reports*, 4:4511, mar 2014.
- [11] Alan Peters, Diana Leahu, Mark B. Moss, and Karen J. McNally. The effects of aging on area 46 of the frontal cortex of the rhesus monkey. *Cerebral Cortex*, 4(6):621–635, 1994.
- [12] Henning Pakkenberg, Birgitte Bo Andersen, Richard S. Burns, and Bente Pakkenberg. A stereological study of substantia nigra in young and old rhesus monkeys. *Brain Research*, 693(1):201–206, 1995.
- [13] R Dee Schramm, Ann Marie Paprocki, and Barry D Bavister. Features associated with reproductive ageing in female rhesus monkeys. *Human Reproduction*, 17(6):1597–603, jun 2002.
- [14] Alan Peters and Claire Folger. A website entitled "The fine structure of the aging brain". *Journal of Comparative Neurology*, 521(6):1203–1206, apr 2013.

- [15] Michael Reed Teague. Image analysis via the general theory of moments. *J. Opt. Soc. Am.*, 70(8):920–930, aug 1980.
- [16] Carsten Steger. On the Calculation of Moments of Polygons. *Tech. Rep. FGBV-96-05*, (August), 1996.
- [17] Alan Peters. The effects of normal aging on myelin and nerve fibers: A review. *Journal of Neurocytology*, 31(8-9):581–593, 2002.
- [18] S. F. Bockman. Generalizing the Formula for Areas of Polygons to Moments. *The American Mathematical Monthly*, 96(2):131, feb 1989.
- [19] H.Eugene Stanley, Sergey V Buldyrev, Luis Cruz, Teresa Gomez-Isla, Shlomo Havlin, Bradley T Hyman, Roger Knowles, Brigita Urbanc, and Claire Wyart. Statistical physics and Alzheimer’s disease. *Physica A: Statistical Mechanics and its Applications*, 249(1-4):460–471, 1998.
- [20] Eckhard Limpert, Werner A. Stahel, and Markus Abbt. Log-normal Distributions across the Sciences: Keys and Clues. *BioScience*, 51(5):341, 2001.
- [21] W. A. H. Rushton. A theory of the effects of fibre size in medullated nerve. *The Journal of Physiology*, 115(1):101–122, 1951.
- [22] S Rao Jammalamadaka and Ashis Sengupta. *Topics in circular statistics*, volume 5. World Scientific, 2001.
- [23] Nicholas I Fisher. *Statistical analysis of circular data*. Cambridge University Press, 1995.
- [24] György Buzsáki and Kenji Mizuseki. The log-dynamic brain: how skewed distributions affect network operations. *Nature reviews. Neuroscience*, 15(4):264–78, 2014.

- [25] Luis Cruz, Brigita Urbanc, Andrew Inglis, Douglas L. Rosene, and H. E. Stanley. Generating a model of the three-dimensional spatial distribution of neurons using density maps. *NeuroImage*, 40(3):1105–1115, 2008.
- [26] A. L. Hodgkin and A. F. Huxley. A quantitative description of membrane current and its application to conduction and excitation in nerve. *Journal of Physiology*, 117(4):500–544, 1952.
- [27] A. Inglis, L. Cruz, D. L. Roe, H. E. Stanley, D. L. Rosene, and B. Urbanc. Automated identification of neurons and their locations. *Journal of Microscopy*, 230(3):339–352, 2008.
- [28] Andrew Inglis. *Measuring Neuron/Glial Cellular Arrangement in the Mammalian Cortex*. PhD thesis, Boston University, 2010.
- [29] Patrick Long and Gabriel Corfas. To learn is to myelinate. *Science*, 346:298, 2014.
- [30] Ian A McKenzie, David Ohayon, Huiliang Li, Joana Paes De Faria, Ben Emery, Koujiro Tohyama, and William D Richardson. Motor skill learning requires active central myelination. *Science*, 346(6207):318–322, 2014.
- [31] Pierre Morell and Richard H Quarles. The Myelin Sheath. In George J Siegel, Bernard W Agranoff, R Wayne Albers, Stephen K Fisher, and Michael D Uhler, editors, *Basic Neurochemistry: Molecular, Cellular and Medical Aspects. 6th edition*. Lippincott-Raven, Philadelphia, 6th edition, 1999.
- [32] Will Z. Morrison. *Understanding the brain through its spatial structure*. PhD thesis, Boston University, 2015.
- [33] Tomás Paus and Roberto Toro. Could Sex Differences in White Matter be Explained by g ratio? *Frontiers in neuroanatomy*, 3(September):14, 2009.

- [34] János A Perge, Jeremy E Niven, Enrico Mugnaini, Vijay Balasubramanian, and Peter Sterling. Why Do Axons Differ in Caliber? *The Journal of Neuroscience*, 32(2):626–638, 2012.
- [35] Alan Peters and Claire Sethares. Is there remyelination during aging of the primate central nervous system? *Journal of Comparative Neurology*, 460(2):238–254, 2003.
- [36] Alan Peters, Claire Sethares, and Ronald J. Killiany. Effects of age on the thickness of myelin sheaths in monkey primary visual cortex. *Journal of Comparative Neurology*, 435(2):241–248, 2001.
- [37] William J. Reed and Barry D. Hughes. From gene families and genera to incomes and internet file sizes: Why power laws are so common in nature. *Physical Review E - Statistical, Nonlinear, and Soft Matter Physics*, 66(6), 2002.
- [38] Sarah R Rudebeck, Jan Scholz, Rebecca Millington, Gustavo Rohenkohl, Heidi Johansen-Berg, and Andy C H Lee. Fornix microstructure correlates with recollection but not familiarity memory. *The Journal of neuroscience : the official journal of the Society for Neuroscience*, 29(47):14987–92, 2009.
- [39] Samuel S.-H. Wang, Jennifer R. Shultz, Mark J. Burish, Kimberly H. Harrison, Patrick R. Hof, Lex C. Towns, Matthew W. Wagers, and Krysta D. Wyatt. Functional trade-offs in white matter axonal scaling. *The Journal of Neuroscience*, 28(15):4047–56, apr 2008.
- [40] James Albert Sethian. *Level set methods and fast marching methods: evolving interfaces in computational geometry, fluid mechanics, computer vision, and materials science*, volume 3. Cambridge University Press, 1999.
- [41] Hans J Johnson, Matthew M McCormick, and Luis Ibáñez. *The ITK Software Guide Book: Design and Functionality*, volume 2. Kitware, Inc., 2015.

- [42] Bastiani, M.J., Harrelson, A.L., Snow, P.M. & Goodman, C.S. Expression of fasciclin I and II glycoproteins on subsets of axon pathways during neuronal development in the grasshopper. *Cell* **48**, 745–755 (1987).
- [43] Cremer, H., Chazal, G., Goridis, C. & Represa, A. NCAM Is Essential for Axonal Growth and Fasciculation in the Hippocampus. *Mol. Cell. Neurosci.* **8**, 323–335 (1997).
- [44] Xue, Y. & Honig, M.G. Ultrastructural observations on the expression of axonin-1: Implications for the fasciculation of sensory axons during axonal outgrowth into the chick hindlimb. *J. Comp. Neurol.* **408**, 299–317 (1999).
- [45] Wilson, S.W., Ross, L.S., Parrett, T. & Easter, S.S. Jr. The development of a simple scaffold of axon tracts in the brain of the embryonic zebrafish, *Brachydanio rerio*. *Development* **108**, 121–145 (1990).
- [46] Scheiffele, P., Fan, J., Choih, J., Fetter, R. & Serafini, T. Neuroligin Expressed in Nonneuronal Cells Triggers Presynaptic Development in Contacting Axons. *Cell* **101**, 657–669 (2000).
- [47] Sánchez, I., Hassinger, L., Paskevich, P.A., Shine, H.D. & Nixon, R.A. Oligodendroglia regulate the regional expansion of axon caliber and local accumulation of neurofilaments during development independently of myelin formation. *J. Neurosci.* **16**, 5095–5105 (1996).
- [48] Gillespie, M.J. & Stein, R.B. The relationship between axon diameter, myelin thickness and conduction velocity during atrophy of mammalian peripheral nerves. *Brain Res.* **259**, 41–56 (1983).
- [49] Ceballos, D., Cuadras, J., Verdú, E. & Navarro, X. Morphometric and ultrastructural changes with ageing in mouse peripheral nerve. *J. Anat.* **195**, 563–576 (1999).

- [50] Elder, G.A., Friedrich, V.L. Jr., Margita, A. & Lazzarini, R.A. Age-related atrophy of motor axons in mice deficient in the mid-sized neurofilament subunit. *J. Cell Biol.* **146**, 181–192 (1999).
- [51] Nielsen, K. & Peters, A. The effects of aging on the frequency of nerve fibers in rhesus monkey striate cortex. *Neurobiol. Aging* **21**, 621–628 (2000).
- [52] Pfefferbaum, A. *et al.* Age-related decline in brain white matter anisotropy measured with spatially corrected echo-planar diffusion tensor imaging. *Magn. Reson. Med.* **44**, 259–268 (2000).
- [53] Cruz, L. *et al.* Age-Related Reduction in Microcolumnar Structure in Area 46 of the Rhesus Monkey Correlates with Behavioral Decline. *Proc. Natl. Acad. Sci. USA* **101**, 15846–15851 (2004).
- [54] Song, S.-K. *et al.* Diffusion tensor imaging detects and differentiates axon and myelin degeneration in mouse optic nerve after retinal ischemia. *NeuroImage* **20**, 1714–1722 (2003).
- [55] Hinton, D.R., Sadun, A.A., Blanks, J.C. & Miller, C.A. Optic-nerve degeneration in Alzheimer's disease. *N. Engl. J. Med.* **315**, 485–487 (1986).
- [56] Moreno, R.D., Inestrosa, N.C., Culwell, A.R. & Alvarez, J. Sprouting and abnormal contacts of nonmedullated axons, and deposition of extracellular material induced by the amyloid precursor protein (APP) and other protease inhibitors. *Brain Res.* **718**, 13–24 (1996).
- [57] Schlaepfer, W.W. & Bunge, R.P. Effects of calcium ion concentration on the degeneration of amputated axons in tissue culture. *J. Cell Biol.* **59**, 456–470 (1973).

- [58] Blight, A.R. & Decrescito, V. Morphometric analysis of experimental spinal cord injury in the cat: the relation of injury intensity to survival of myelinated axons. *Neuroscience* **19**, 321–341 (1986).
- [59] Xu, X.M., Guénard, V., Kleitman, N., Aebischer, P. & Bunge, M.B. A combination of BDNF and NT-3 promotes supraspinal axonal regeneration into Schwann cell grafts in adult rat thoracic spinal cord. *Exp. Neurol.* **134**, 261–272 (1995).
- [60] Aguayo, A.J., David, S. & Bray, G.M. Influences of the glial environment on the elongation of axons after injury: transplantation studies in adult rodents. *J. Exp. Biol.* **95**, 231–240 (1981).
- [61] Kao, C.C., Chang, L.W. & Bloodworth, J.M.B. Jr. Axonal regeneration across transected mammalian spinal cords: an electron microscopic study of delayed microsurgical nerve grafting. *Exp. Neurol.* **54**, 591–615 (1977).
- [62] Noseworthy, J.H., Lucchinetti, C., Rodriguez, M. & Weinshenker, B.G. Multiple sclerosis. *N. Engl. J. Med.* **343**, 938–952 (2000).
- [63] Raine, C.S., Hummelgard, A., Swanson, E. & Bornstein, M.B. Multiple sclerosis: serum-induced demyelination in vitro. A light and electron microscope study. *J. Neurol. Sci.* **20**, 127–148 (1973).
- [64] Trapp, B.D. *et al.* Axonal transection in the lesions of multiple sclerosis. *N. Engl. J. Med.* **338**, 278–285 (1998).
- [65] Wujek, J.R. *et al.* Axon loss in the spinal cord determines permanent neurological disability in an animal model of multiple sclerosis. *J. Neuropathol. Exp. Neurol.* **61**, 23–32 (2002).
- [66] Stankovic, R.K., Shingde, M. & Cullen, K.M. The experimental toxicology of metallic mercury on the murine peripheral motor system: a novel method of

- assessing axon calibre spectra using the phrenic nerve. *J. Neurosci. Methods* **147**, 114–125 (2005).
- [67] Stankovic, R. Atrophy of large myelinated motor axons and declining muscle grip strength following mercury vapor inhalation in mice. *Inhal. Toxicol.* **18**, 57–69 (2006).
- [68] Ayrançı, E., Altunkaynak, B.Z., Aktaş, A., Rağbetli, M.Ç. & Kaplan, S. Prenatal exposure of diclofenac sodium affects morphology but not axon number of the median nerve of rats. *Folia Neuropathol.* **51**, 76–86 (2013).
- [69] Giese, K.P., Martini, R., Lemke, G., Soriano, P. & Schachner, M. Mouse P0 gene disruption leads to hypomyelination, abnormal expression of recognition molecules, and degeneration of myelin and axons. *Cell* **71**, 565–576 (1992).
- [70] Readhead, C. *et al.* Expression of a myelin basic protein gene in transgenic shiverer mice: correction of the dysmyelinating phenotype. *Cell* **48**, 703–712 (1987).
- [71] Craddock, R.C., Holtzheimer, P.E., Hu, X.P. & Mayberg, H.S. Disease state prediction from resting state functional connectivity. *Magn. Reson. Med.* **62**, 1619–1628 (2009).
- [72] Millán, J., Franzé, M., Mouriño, J., Cincotti, F. & Babiloni, F. Relevant EEG features for the classification of spontaneous motor-related tasks. *Biol. Cybern.* **86**, 89–95 (2002).
- [73] Cui, Y. *et al.* Identification of conversion from mild cognitive impairment to Alzheimer’s disease using multivariate predictors. *PLoS ONE* **6**, e21896 (2011).
- [74] Celebi, M.E. *et al.* A methodological approach to the classification of dermoscopy images. *Comput. Med. Imaging Graph.* **31**, 362–373 (2007).

- [75] Blum, A.L. & Langley, P. Selection of relevant features and examples in machine learning. *Artif. Intell.* **97**, 245–271 (1997).
- [76] Gaffan, D. Recognition impaired and association intact in the memory of monkeys after transection of the fornix. *J. Comp. Physiol. Psychol.* **86**, 1100–1109 (1974).
- [77] Costa, L. da F. & Cesar, R.M. Jr. *Shape Classification and Analysis: Theory and Practice*. (CRC Press, 2nd edition, Boca Raton, FL, USA, 2009).
- [78] Witten, I.H., Frank, E. & Hall, M.A. *Data Mining: Practical Machine Learning Tools and Techniques*. (Morgan Kaufmann, 3rd edition, San Francisco, CA, USA, 2011).
- [79] Duda, R.O., Hart, P.E. & Stork, D.G. *Pattern Classification*. (Wiley-Interscience, 2nd edition, 2000).
- [80] Costa, L. da F., Rocha, F. & de Lima, S.M.A. Characterizing polygonality in biological structures. *Phys. Rev. E* **73**, 011913 (2006).
- [81] Bellman, R. *Dynamic Programming*. (Dover Publications, Mineola, NY, USA, 2003).
- [82] Jolliffe, I.T. *Principal component analysis*. (Springer, 2nd edition, New York, NY, USA, 2002).
- [83] Russell, S. & Norvig, P. *Artificial Intelligence: A Modern Approach*. (Prentice Hall, 3rd edition, Upper Saddle River, NJ, USA, 2009).
- [84] Fukunaga, K. *Introduction to Statistical Pattern Recognition*. (Academic Press, 2nd edition, San Diego, CA, USA, 1990).
- [85] Everitt, B.S., Landau, S., Leese, M. & Stahl, D. *Cluster analysis*. (Wiley, 5th edition, Chichester, West Sussex, UK, 2011).

- [86] Canny, J. A Computational Approach To Edge Detection. *IEEE Trans. Pattern Anal. Mach. Intell.* **8**, 679–698 (1986).
- [87] Pakkenberg, B. & Gundersen, H.J.G. Neocortical neuron numbers in humans: effect of sex and age. *J. Comp. Neurol.* **384**, 312–320 (1997).
- [88] Tang, Y., Nyengaard, J.R., Pakkenberg, B. & Gundersen, H.J.G. Age-induced white matter changes in the human brain: a stereological investigation. *Neurobiol. Aging* **18**, 609–615 (1997).
- [89] Marnier, L., Nyengaard, J.R., Tang, Y. & Pakkenberg, B. Marked loss of myelinated nerve fibers in the human brain with age. *J. Comp. Neurol.* **462**, 144–152 (2003).
- [90] Kingman, J.F.C. *Poisson Processes*. (Oxford University Press, New York, USA, 1993).
- [91] Percus, A.G. & Martin, O.C. Scaling universalities of kth-nearest neighbor distances on closed manifolds. *Adv. Appl. Math.* **21**, 424–436 (1998).
- [92] Olver, F.W.J., Lozier, D.W., Boisvert, R.F. & Clark, C.W. *NIST Handbook of Mathematical Functions*. (Cambridge University Press, New York, USA, 2010).
- [93] Kohavi, R. & John, G.H. Wrappers for feature subset selection. *Artif. Intell.* **97**, 273–324 (1997).

Curriculum Vitae

João Ricardo Lemos Rodrigues dos Santos

Boston University, Physics Department
590 Commonwealth Avenue
Boston, Massachusetts 02215 USA

Cell: 617-334-5626
Telephone: 617-353-9459
E-mail: jrsantos@bu.edu

EDUCATION

- 2016, Ph.D. Physics, Boston University, Boston, MA, USA
Advisors: H. Eugene Stanley & Doug L. Rosene
Dissertation: *Aging Effects on the Statistical and Structural Properties of the Fornix of the Brain.*
- 2010, M.A. Physics, Boston University, Boston, MA, USA
- 2006, B.S. Physics, Universidade do Minho, Braga, Portugal
Diploma Thesis: *Study of Disorder Effects in Graphene Sheets.*
Investigation Report: *Modeling of the anti-Stokes Photoluminescence of Quantum Dots in Colloidal Solutions.*

RESEARCH AND TEACHING EXPERIENCE

- May '10 – Present, Research Assistant, Boston University.
- Sep '07 – Dec '12, Teaching Assistant, Boston University.
- Apr '07 – Aug '07, Research Scientist, University of Fribourg, Switzerland.

- Oct '06 – Dec '06, Physics and Mathematics Teacher, University of Minho, Portugal.

RESEARCH INTERESTS

- Data Science: data collection, modeling, and data analysis.
- Application of Statistical Physics to Neuroscience.
- Condensed Matter Physics: theoretical studies of electronic properties of Graphene and semiconductor quantum dots.

PUBLICATIONS

1. **Santos, J. R.**, Comin, C. H., Rosene, D. L., Gabrielli, A., Costa, L. da F. & Stanley, H. E. *Effects of aging on myelinated nerve fibers in the primate fornix*. In preparation (2016).
2. Comin, C. H., **Santos, J. R.**, Corradini, D., Morrison, W., Curme, C., Rosene, D. L., Gabrielli, A., Costa, L. da F. & Stanley, H. E. *Statistical physics approach to quantifying differences in myelinated nerve fibers*. Sci. Rep. 4, 4511 (2014).
3. Malainho, E., **Santos, J. R.**, Vasilevskiy, M. I., Filonovich, S. A., Rakovich, Y. P. & Rogach, A. *Cascade upconversion of photoluminescence in ensembles of II-VI semiconductor nanocrystals*. Phys. Status Solidi C 7, 1517–1519 (2010).
4. **Santos, J. R.**, Vasilevskiy, M. I. & Filonovich, S. A. *Cascade upconversion of photoluminescence in quantum dot ensembles*. Phys. Rev. B 78, (2008).
5. Peres, N. M. R., Klironomos, F. D., Tsai, S.-W., **Santos, J. R.**, Lopes dos Santos, J. M. B. & Castro Neto, A. H. *Electron waves in chemically substituted graphene*. Europhysics Letters 80, 67007 (2007).

PRESENTATIONS

- 2015, 2015 Graduate Research Symposium, Boston, MA, USA
Application of feature recognition and statistical physics methods to quantify age-related changes in myelinated nerve fibers in monkey brain.
- 2014, Neuroscience 2014 Annual Meeting, Washington, D.C., USA
Application of feature recognition and statistical physics methods to quantify age-related changes in myelinated nerve fibers in monkey brain.
- 2007, ICPS 2007 – International Conference of Physics Students, London, UK
Disorder Effects in Graphene.
- 2007, IX ENEF – Encontro Nacional de Estudantes de Física, Faro, Portugal
Grafeno: Electrodinâmica Quântica na ponta de um lápis.
- 2006, 15th Physics National Conference, Aveiro, Portugal
Propriedades Electrónicas do Grafeno.
- 2006, ICPS 2006 – International Conference of Physics Students, Bucharest, Romania
Modeling of the anti-Stokes Photoluminescence of Quantum Dots in Colloidal Solutions.
- 2006, VIII ENEF – Encontro Nacional de Estudantes de Física, Braga, Portugal
Modelização da Fotoluminescência anti-Stokes em Soluções Coloidais de Pontos Quânticos.

AWARDS

- NSF EAGER grant for Initiative for Physics and Mathematics of Neural Systems, 2014 – 2016.
- Student Scholarship from Fundação para a Ciência e a Tecnologia, Portugal, 2008 – 2012.
- Research Scholarship, University of Fribourg, Switzerland, 2007.
- Winner of the best oral communication in the VIII ENEF, 2006.
- Prize for Scholar Merit, granted by the University of Minho, 2003 – 2006.

SKILLS

- *Programming*: Python, C, Fortran, bash; basic competence in R and machine learning.
- *Computer*: GNU/Linux, Windows, Microsoft Office, and Latex.
- Collecting, parsing, and analyzing large data in research projects, modeling complex systems, and summarizing information and results.
- Communicating challenging topics to varied audiences, including undergraduate students, grant reviewers, and the scientific community.
- Leading and organizing an international research team and events for the Portuguese American Post-Graduate Society.

LANGUAGES

- *English*: speak, read, and write fluently.
- *Portuguese*: native language.
- *Spanish*: speak and read with intermediate competence.
- *French*: speak, read, and write with basic competence.